NASA Contractor Report 195008

Laminar and Turbulent Flow Computations of Type IV Shock-Shock Interference Aerothermal Loads Using Unstructured Grids

Gururaja R. Vemaganti
Lockheed Engineering & Sciences Company, Hampton, VA

Contract NAS1-19000

October 1994

National Aeronautics and Space Administration
Langley Research Center
Hampton, Virginia 23681-0001

Foreword

This document was prepared by Lockheed Engineering & Sciences Company, Langley Program Office, for the National Aeronautics and Space Administration, Langley Research Center, Hampton, Virginia. The work was performed under contract NAS1-19000. Dr. Allan R. Wieting was the NASA Technical Monitor for this task.

Abstract

This report presents computations for the Type IV shock-shock interference flow under laminar and turbulent conditions using unstructured grids. Mesh adaptation was accomplished by remeshing, refinement and mesh movement. Two two-equation turbulence models were used to analyze turbulent flows. The mean flow governing equations and the turbulence governing equations are solved in a coupled manner. The solution algorithm and the details pertaining to its implementation on unstructured grids are described. Computations were performed at two different freestream Reynolds numbers at a freestream Mach number of 11. Effects of the variation in the impinging shock location are studied. The comparison of the results in terms of wall heat flux and wall pressure distributions is presented.

Nomenclature

A	Jacobian matrix
a	speed of sound, m/sec
B	matrix associated with the viscous fluxes
BT	boundary term
C	constant
C_f	local skin friction coefficient
C_p	specific heat at constant pressure, J/kg-K
C_v	specific heat at constant volume, J/kg-K
E	total energy, J/kg
F	inviscid flux
f	damping function
G	viscous flux
h	specific enthalpy, J/kg

k	turbulent kinetic energy, J/kg
M	Mach number; mass matrix
N	element shape functions; number of sides
n	direction cosines
P	production terms
p	pressure, N/m^2
Pr	Prandtl number
q	heat transfer rate, MW/m^2
q_o	stagnation heat flux in the undisturbed flow, MW/m^2
r	radius of the cylinder, in
R	eigenvector matrix
Re	Reynolds number
S	source terms
T	temperature, K
t	time, sec
U	conservation variable
u	component of velocity in x-direction; velocity component in indicial notation, m/sec
v	component of velocity in y-direction, m/sec
x,y	coordinates of the reference frame

GREEK SYMBOLS

α	constant
δ	Kronecker delta; length of an element side; boundary layer thickness
ε	turbulent dissipation rate, m^2/sec^3
$\in$	eigenvalue limiter
γ	ratio of specific heats
Γ	edge of an element
λ	eigenvalue
μ	viscosity, $N\text{-}s/m^2$
ν	kinematic viscosity, m^2/sec
θ	angle
ρ	density, kg/m^3
σ	normal stress, N/m^2
τ	shear stress, N/m^2
ω	specific dissipation rate, 1/sec
Ω	area of an element, m^2

SUBSCRIPTS

i,j,k	indices of notation
inf	freestream conditions
e	element
L	left value; lumped value

n	normal direction
o	stagnation value
peak	maximum
s	side
T	turbulence quantity
w	wall
x,y	coordinate axes
∞	freestream

SUPERSCRIPTS

*	current value
m	time step index
+	near wall non-dimensionalization

Introduction

Intense aerothermal loads that result from shock-shock interferences (especially Type III and Type IV interferences) on a hypersonic vehicle are critical for design purposes. Computational methods are being developed at the NASA Langley Research Center to accurately predict these loads. These efforts have led to the development of LARCNESS (acronym for Langley Adaptive Remeshing Code NaviEr Stokes Solver) which is a software package that includes a flow solver based on a point-implicit, upwind algorithm, and an unstructured mesh generator based on an adaptive remeshing technique. LARCNESS has been used successfully in resolving complicated flow features that result from shock-shock interferences under laminar flow conditions. The details of the algorithm and the computational results are found in Reference 1.

In a typical Type IV shock-shock interference problem a supersonic jet is produced which impinges on the body as shown in Fig. 1. This impingement causes highly localized peaks of wall pressures and wall heat fluxes. LARCNESS was used to analyze this problem computationally using unstructured grids {Ref. 1}. There is some experimental evidence to show that the shear layers surrounding the supersonic jet are turbulent during experiments {Ref. 2}. This indicated a need for implementation of a turbulence

model in LARCNESS to investigate the turbulence effects, and this effort addressed this problem.

Algebraic turbulence models (mixing-length type) have been successfully used in compressible turbulent flow computations (for example, see Ref. 3). However, their application is limited to wall bounded flows using structured grids. They also lack generality in the context of application to complicated geometries and complex flow fields such as shock waves, jets and shear layers. On the other hand, the two-equation models are not limited to wall bounded flows, and offer the flexibility of dealing with complex flow features using unstructured grids. In general, these models introduce two turbulence parameters, one for the turbulence kinetic energy, k, and the other for the turbulence length scale determining parameter (for example, the turbulent dissipation rate, ε). These turbulence parameters which define the turbulent viscosity in the flow field are governed by two partial differential equations that must be solved together with the mean flow equations. Although there are several higher-order turbulence models like the Reynolds-stress models, they are still in the developmental stage, leaving the most popular two-equation models for practical applications.

The two-equation model was first developed by Jones and Launder {Ref. 4}. Several modifications to this model have been proposed recently, and concise reviews on these models may be found in References 5, 6 & 7. Among the many two-equation models available, only a few are capable of modeling high speed compressible turbulence. One such model is the compressible k-ε model with near-wall damping functions developed by Zhang, et al. {Ref. 8}. This is the most widely used two-equation model in the literature, and it has been very successful for a large variety of different flow situations, including free shear layers. However, the k-ε model suffers from several shortcomings.

Some of these shortcomings include lack of sensitivity to adverse pressure gradients, problems related to numerical stiffness in the near-wall regions and in some cases underprediction of wall heat fluxes. {Ref. 9 & 10}.

On the other hand, another very successful two-equation turbulence model, the k-ω model originally developed by Wilcox {Ref. 11} is robust and accurate in predicting near wall turbulence even under adverse pressure gradients. The major shortcoming of the k-ω model is its high sensitivity to freestream conditions and hence its inability to predict free shear layers accurately. A combination of the k-ε model and the k-ω model appears to eliminate each other's shortcomings and give rise to a better turbulence model {Ref. 12}. Recently several zonal approaches combining these models were successfully attempted in solving high speed flow problems {Ref. 12 & 13} and a similar approach is used in the current work. Since, in the present code, structured grids are used near the wall and unstructured grids elsewhere, the k-ω model is used in the structured grid portion of the mesh and the k-ε model is used in the unstructured grid portion of the mesh.

Some work has been reported in the literature regarding the implementation of two-equation turbulence models for compressible flow in the context of unstructured grids. Marcum and Agarwal {Ref. 14}, implemented the k-ε model in a Galerkin finite-element procedure for solving the Reynolds-averaged mean flow equations. Mavriplis {Ref. 15} implemented a compressible version of the k-ε model in a multi-stage Runge-Kutta time-stepping scheme using a multigrid strategy on unstructured grids. In both of these papers however, the mean flow equations and the turbulence equations were solved in an uncoupled manner. Morrison {Ref. 16} implemented the k-ε model proposed by Zhang, et al. {Ref. 8} in a cell-centered finite-volume technique, using the Roe's flux difference splitting technique in a coupled

manner (solving all the governing equations simultaneously) on structured grids. In the present work, unstructured grids are employed, and both methods of solving (coupled and uncoupled methods) the governing equations are investigated.

The purpose of this report is to present the laminar and turbulent flow computations using two-equation turbulence models in association with an unstructured grid solver for the Type IV shock-shock interference problem. First the turbulence models, along with some details regarding its implementation into the LARCNESS code, are presented. The computational results for the shock-shock interference at two different freestream Reynolds numbers in a Mach 11 flow over a 3 inch cylinder are presented. A comparison of the laminar flow computations with the turbulent flow computations are made. Conclusions are drawn based on these studies.

Governing Equations and the Turbulence Models

The basic governing equations for the mean flow are the Favre-averaged Reynolds equations along with Boussinesq approximation and are given as follows:

$$\frac{\partial \bar{\rho}}{\partial t} + \frac{\partial (\bar{\rho}\tilde{u}_j)}{\partial x_j} = 0 \tag{1}$$

$$\frac{\partial (\bar{\rho}\tilde{u}_i)}{\partial t} + \frac{\partial (\bar{\rho}\tilde{u}_i\tilde{u}_j)}{\partial x_j} = -\frac{\partial \bar{p}}{\partial x_i} + \frac{\partial}{\partial x_j}\left((\bar{\mu} + \bar{\mu_T})\left(\frac{\partial \tilde{u}_i}{\partial x_j} + \frac{\partial \tilde{u}_j}{\partial x_i}\right) - \frac{2}{3}(\bar{\mu} + \bar{\mu_T})\frac{\partial \tilde{u}_k}{\partial x_k} + \frac{2}{3}\bar{\rho}\tilde{k}\delta_{ij}\right) \tag{2}$$

$$\frac{\partial(\overline{\rho}\widetilde{E})}{\partial t}+\frac{\partial(\overline{\rho}\widetilde{E}\widetilde{u}_j)}{\partial x_j}=\frac{\partial\left(\left(\frac{\overline{\mu}}{Pr}+\frac{\overline{\mu_T}}{Pr_T}\right)\frac{\partial\widetilde{h}}{\partial x_j}\right)}{\partial x_j}-\frac{\partial(\overline{p}\widetilde{u}_j)}{\partial x_j}$$
$$+\frac{\partial u_j\left((\overline{\mu}+\overline{\mu_T})\left(\frac{\partial\widetilde{u}_i}{\partial x_j}+\frac{\partial\widetilde{u}_j}{\partial x_i}\right)-\frac{2}{3}(\overline{\mu}+\overline{\mu_T})\frac{\partial\widetilde{u}_k}{\partial x_k}+\frac{2}{3}\overline{\rho}\widetilde{k}\delta_{ij}\right)}{\partial x_j}$$
$$+\frac{\partial\left(\left(\overline{\mu}+\frac{\overline{\mu_T}}{\sigma_k}\right)\frac{\partial\widetilde{k}}{\partial x_j}\right)}{\partial x_j} \qquad (3)$$

("tilde" over-bar represents Favre mass averaged quantity, and plain over-bar represents the time averaged quantity). In the above equations, $\overline{\mu_T}$ is the turbulent viscosity, $\overline{Pr_T}$ is the turbulent Prandtl number and $\widetilde{k}$ is the kinetic energy of turbulence given by

$$\widetilde{k}=\overline{\rho u''_i u''_i}/2\overline{\rho} \qquad (4)$$

The k-ε model

In the k-ε model, the turbulent viscosity is expressed in terms of turbulent kinetic energy $\widetilde{k}$, and the turbulence dissipation rate $\widetilde{\varepsilon}$ as follows:

$$\overline{\mu_T}=\frac{C_\mu\overline{\rho}\widetilde{k}^2}{\widetilde{\varepsilon}} \qquad (5)$$

where C_μ is a constant and the dissipation rate $\widetilde{\varepsilon}$ is expressed as follows:

$$\widetilde{\varepsilon}=\frac{\overline{\rho\nu\frac{\partial u''_i\partial u''_i}{\partial x_j\,\partial x_j}}}{\overline{\rho}} \qquad (6)$$

This model introduces two more unknowns in the original set of governing equations, i.e., the turbulent kinetic energy $(\widetilde{k})$ and the turbulence dissipation rate $(\widetilde{\varepsilon})$, which are governed by the following partial differential equations expressed in the conservation form :

$$\frac{\partial(\overline{\rho}\widetilde{k})}{\partial t}+\frac{\partial(\overline{\rho}\widetilde{k}\widetilde{u}_j)}{\partial x_j}=P_k-\overline{\rho}\widetilde{\varepsilon}(1+\alpha M_T^2)+\frac{\partial\left(\left(\overline{\mu}+\frac{\overline{\mu_T}}{\sigma_k}\right)\frac{\partial\widetilde{k}}{\partial x_j}\right)}{\partial x_j} \qquad (7)$$

$$\frac{\partial(\overline{\rho\varepsilon})}{\partial t}+\frac{\partial(\overline{\rho\varepsilon}\tilde{u}_j)}{\partial x_j}=C_1\frac{\tilde{\varepsilon}}{\tilde{k}}P_k-\overline{\rho}\tilde{\varepsilon}\left(C_2\frac{\tilde{\varepsilon}}{\tilde{k}}\right)+\frac{\partial\left(\left(\overline{\mu}+\frac{\overline{\mu_T}}{\sigma_\varepsilon}\right)\frac{\partial\tilde{\varepsilon}}{\partial x_j}\right)}{\partial x_j} \tag{8}$$

In the above equations, P_k represents a production term given as follows

$$P_k=-\overline{\rho u''_i u''_j}\frac{\partial\tilde{u}_j}{\partial x_j}=\overline{\mu}_T\left[\frac{1}{2}\left(\frac{\partial\tilde{u}_i}{\partial x_j}+\frac{\partial\tilde{u}_j}{\partial x_i}\right)^2-\frac{2}{3}\left(\frac{\partial\tilde{u}_k}{\partial x_k}\right)^2-\frac{2}{3}\overline{\rho}\tilde{k}\frac{\partial\tilde{u}_k}{\partial x_k}\right] \tag{9}$$

where C_1, C_2, σ_k, σ_ε, and α are constants, and M_T is the local turbulent Mach number defined in terms of turbulence kinetic energy and local speed of sound a, as follows:

$$M_T=\sqrt{\frac{2\tilde{k}}{a^2}} \tag{10}$$

The constants used in Eqn. (7) and (8) are given below (11)

$$C_1 = 1.44$$

$$C_2 = 1.92$$

$$\sigma_T = 1.0$$

$$\sigma_\varepsilon = 1.0$$

$$\alpha = 0.5$$

The k-ω model

In the k-ω model, the turbulent viscosity is expressed in terms of turbulent kinetic energy $\tilde{k}$, and the specific dissipation rate $\tilde{\omega}$ as follows:

$$\overline{\mu_T}=\frac{\overline{\rho}\tilde{k}}{\tilde{\omega}} \tag{12}$$

where $\tilde{\omega}$ is defined as

$$\overline{\omega}=\frac{\tilde{\varepsilon}}{C_\mu\tilde{k}} \tag{13}$$

The governing equation for the turbulent kinetic energy $\tilde{k}$ in this model is the same as the governing equation in the k-ε model except the dissipation terms are expressed in terms of the specific dissipation rate $\tilde{\omega}$, and given as follows:

$$\frac{\partial(\overline{\rho}\widetilde{k})}{\partial t}+\frac{\partial(\overline{\rho}\widetilde{k}\widetilde{u}_j)}{\partial x_j}=P_k-C_\mu\,\overline{\rho}\widetilde{\omega}\widetilde{k}(1+\alpha M_T^2)+\frac{\partial\left(\left(\overline{\mu}+\dfrac{\overline{\mu_T}}{\sigma_k}\right)\dfrac{\partial\widetilde{k}}{\partial x_j}\right)}{\partial x_j} \tag{14}$$

The various constants in Eqns. (13) and (14) are the same as the constants in the k-ε model. The governing equation for $\widetilde{\omega}$, the specific dissipation rate, is given as follows:

$$\frac{\partial(\overline{\rho}\widetilde{\omega})}{\partial t}+\frac{\partial(\overline{\rho}\widetilde{\omega}\widetilde{u}_j)}{\partial x_j}=\gamma_2\frac{\widetilde{\omega}}{\widetilde{k}}P_k-\beta_2\left(\overline{\rho}\,\widetilde{\omega}^2\right)+\frac{\partial\left(\left(\overline{\mu}+\dfrac{\overline{\mu_T}}{\sigma_\omega}\right)\dfrac{\partial\widetilde{\omega}}{\partial x_j}\right)}{\partial x_j} \tag{15}$$

where

$$\gamma_2=C_1-1;\ \beta_2=C_\mu\left(C_2-\left(1+\alpha M_T^2\right)\right) \tag{16}$$

In order to incorporate the low turbulent Reynolds number effects (that are present in the laminar sublayer region near a solid wall) into the turbulence model, a set of damping functions as suggested in Ref. 11 are implemented in the current model.

The cross-diffusion term

Since the turbulence dissipation rate, $\widehat{\varepsilon}$, is related to the specific dissipation rate $\widetilde{\omega}$, equation (8) can be written in terms of $\widetilde{\omega}$ as follows:

$$\frac{\partial(\overline{\rho}\widetilde{\omega})}{\partial t}+\frac{\partial(\overline{\rho}\widetilde{\omega}\widetilde{u}_j)}{\partial x_j}=\gamma_2\frac{\widetilde{\omega}}{\widetilde{k}}P_k-\beta_2\left(\overline{\rho}\,\widetilde{\omega}^2\right)+\frac{\partial\left(\left(\overline{\mu}+\dfrac{\overline{\mu_T}}{\sigma_\omega}\right)\dfrac{\partial\widetilde{\omega}}{\partial x_j}\right)}{\partial x_j}+2\frac{\partial\widetilde{k}\partial\widetilde{\omega}}{\partial x_j\partial x_j}\left(\frac{\mu}{\widetilde{k}}+\frac{\rho}{\sigma_\omega\,\widetilde{\omega}}\right) \tag{17}$$

Comparing Eqns. (8) and (17) it can be easily noticed that the difference between the $\widehat{\varepsilon}$ equation expressed in terms of $\widetilde{\omega}$ and the $\widetilde{\omega}$ equation is the cross-diffusion term that appears at the end of right-hand-side of Eqn. (17). In other words dropping of the cross-diffusion term from the transformed $\widehat{\varepsilon}$ equation results exactly in the governing equation for $\widetilde{\omega}$. Since the governing equation for $\widehat{k}$ is the same in both the models many of the shortcomings of the k-ε model

are attributed {Refs. 12 & 17} to the presence of this cross-diffusion term in the $\tilde{\varepsilon}$ governing equation . Conversely, the shortcomings of the k-ω model are generally attributed to the absence of this cross-diffusion term in the $\tilde{\omega}$ governing equation. In the zonal approach, the formulation is made according to the k-ω model and the cross-diffusion term is introduced in the $\tilde{\omega}$ governing equation in the regions where the k-ε model is employed through a blending function. In the current formulation, $\tilde{\omega}$ is used as a length scale turbulence parameter and the cross-diffusion term is introduced into the $\tilde{\omega}$ governing equation to recover the k-ε model wherever needed.

Implementation in LARCNESS Code

The set of governing equations are solved using an upwind, point-implicit, cell-centered scheme based on Roe's averaging. The point-implicit time marching procedure for the Navier-Stokes equations is given in Ref. 1. Extension of this solution procedure for Reynolds averaged mean flow equations was accomplished by including additional terms in the mean flow equations. In the current approach the four mean flow equations and the two turbulence governing equations are solved in a coupled manner, as proposed in Ref. 16.

The details of the solution procedure for the coupled set of governing equations are as follows. For the sake of simplicity, over-bars are eliminated in the following discussion. The set of governing equations can be written in the conservation form as

$$\frac{\partial \{U\}}{\partial t} + \frac{\partial \{F\}_i}{\partial x_i} = -\frac{\partial \{G\}_i}{\partial x_i} + \{S\} \qquad (18)$$

where $\{U\}$ is the vector of conservation variables, $\{F\}$ is the inviscid flux vector, $\{G\}$ is the viscous flux vector, and $\{S\}$ is the vector containing the source terms

(source terms exist only in the turbulence equations comprising of production and dissipation or destruction terms). These vectors are given as follows:

$$\{U\} = \begin{Bmatrix} \rho \\ \rho u \\ \rho v \\ \rho E \\ \rho k \\ \rho \omega \end{Bmatrix} \tag{19}$$

and,

$$\{F_1\} = \begin{Bmatrix} \rho u \\ \rho u^2 + p \\ \rho u v \\ (\rho E + p) u \\ \rho u k \\ \rho u \omega \end{Bmatrix}; \quad \{F_2\} = \begin{Bmatrix} \rho v \\ \rho u v \\ \rho v^2 + p \\ (\rho E + p) v \\ \rho v k \\ \rho v \omega \end{Bmatrix};$$

$$\{G_1\} = -\begin{Bmatrix} 0 \\ \sigma_{xx} \\ \tau_{xy} \\ u\,\sigma_{xx} + v\,\tau_{xy} - q_x + D_{kx} \\ D_{kx} \\ D_{\omega x} \end{Bmatrix}; \quad \{G_2\} = -\begin{Bmatrix} 0 \\ \tau_{yx} \\ \sigma_{yy} \\ u\,\tau_{yx} + v\,\sigma_{yy} - q_y + D_{ky} \\ D_{ky} \\ D_{\omega y} \end{Bmatrix}; \tag{20}$$

and,

$$\{S\} = \begin{Bmatrix} 0 \\ 0 \\ 0 \\ 0 \\ P_k - C_\mu \rho \omega k \left(1 + \alpha M_T^2\right) \\ \gamma_2 \dfrac{\omega}{k} P_k - \beta_2 \rho \omega^2 \end{Bmatrix} \tag{21}$$

where σ_{xx}, σ_{yy} and τ_{xy} are the stress components, D_{kx}, D_{ky}, $D_{\omega x}$, and $D_{\omega y}$ are the diffusion terms in the turbulence equations, and q_x and q_y are the components of the heat-flux vector. A calorically perfect gas is assumed.

The stress components are given by

$$\sigma_{xx} = \frac{2}{3}(\mu + \mu_T)\left[2\frac{\partial u}{\partial x} - \frac{\partial v}{\partial y}\right] + \frac{2}{3}\rho k \tag{22}$$

$$\tau_{xy} = \tau_{yx} = (\mu + \mu_T)\left[\frac{\partial u}{\partial y} + \frac{\partial v}{\partial x}\right] \tag{23}$$

and

$$\sigma_{yy} = \frac{2}{3}(\mu + \mu_T)\left[2\frac{\partial v}{\partial y} - \frac{\partial u}{\partial x}\right] + \frac{2}{3}\rho k \tag{24}$$

The components of the heat-flux vector are given by

$$q_x = -C_P\left(\frac{\mu}{Pr} + \frac{\mu_T}{Pr_T}\right)\frac{\partial T}{\partial x} \tag{25}$$

and

$$q_y = -C_P\left(\frac{\mu}{Pr} + \frac{\mu_T}{Pr_T}\right)\frac{\partial T}{\partial y} \tag{26}$$

The diffusion terms in the turbulence equations are given as follows:

$$D_{kx} = \left(\mu + \frac{\mu_T}{\sigma_k}\right)\frac{\partial k}{\partial x} \quad ; D_{ky} = \left(\mu + \frac{\mu_T}{\sigma_k}\right)\frac{\partial k}{\partial y} \tag{27}$$

and

$$D_{\omega x} = \left(\mu + \frac{\mu_T}{\sigma_\omega}\right)\frac{\partial \omega}{\partial x} \quad ; D_{\omega y} = \left(\mu + \frac{\mu_T}{\sigma_\omega}\right)\frac{\partial \omega}{\partial y} \tag{28}$$

The solution domain is discretized spatially into an unstructured grid of triangular and quadrilateral elements, and the set of governing equations is solved subject to appropriate initial and boundary conditions. The governing equations for each element can be expressed in an integral manner as given below.

$$\int_{\Omega_e} \frac{\partial \{U\}}{\partial t} d\Omega = \int_{\Omega_e} \left(\frac{\partial \{G\}_j}{\partial x_j} - \frac{\partial \{F\}_j}{\partial x_j} \right) d\Omega + \int_{\Omega_e} \{S\} d\Omega \qquad (29)$$

where Ω_e is the area of the element. Assuming a piecewise constant distribution of the unknowns U and linearizing U with respect to t, Eqn. (29) can be rewritten as shown below.

$$\frac{\{U_e\}^{m+1} - \{U_e\}^m}{\Delta t} = \frac{1}{\Omega_e} \left(\int_{\Omega_e} \left(\frac{\partial \{G\}_j}{\partial x_j} - \frac{\partial \{F\}_j}{\partial x_j} \right) d\Omega + \int_{\Omega_e} \{S\} d\Omega \right) \qquad (30)$$

where U_e represents element level unknowns and m denotes the time level. By application of the divergence theorem to the flux terms on the left-hand-side, Eqn. (30) can be written as follows:

$$\int_{\Omega_e} \left(\frac{\partial \{G\}_j}{\partial x_j} - \frac{\partial \{F\}_j}{\partial x_j} \right) d\Omega = \int_{\Gamma_e} (\{G_n\} - \{F_n\})\, d\Gamma \qquad (31)$$

where Γ_e is the element boundary and the subscript n denotes the flux normal to the element sides.

Assuming the viscous fluxes to be a constant along the sides of an element and the source terms to be constant within the element, Eqn. (31) can be written as

$$\{\Delta U_e\}^m = \frac{\Delta t}{\Omega_e} \left\{ \sum_{s=1}^{nside} \delta_s \left[\{G_n\}^{m+1} - \{F_n\}^{m+1} \right]_s + \Omega_e \{S_e\}^{m+1} \right\} \qquad (32)$$

where δ_s is the length of the side under consideration, and *nside* denotes the total number of sides in the element. In Eqn. (32) G_n and F_n represent the viscous and inviscid fluxes respectively, and S_e denotes the source terms. Computation of these quantities is discussed in the following section.

Treatment of the Fluxes

The inviscid flux vector F_n appearing in Eqn. (32) is replaced by a numerical flux given by

$$\{F_n\} = \frac{1}{2}[\{F_R\} + \{F_L\} - [|A|]\,(\{U_R\} - \{U_L\})] \tag{33}$$

where subscripts R and L denote the right and left values with respect to the side s, and the term $[|A|]\,(\{U_R\} - \{U_L\})$ is the first-order dissipation term as suggested by Gnoffo {Ref. 18}. The matrix $[A]$ is the Jacobian of the inviscid flux vector evaluated at the Roe's average state {Ref. 19}, and has the property

$$\{F_R\} - \{F_L\} = [A]\,(\{U_R\} - \{U_L\}) \tag{34}$$

This matrix can be factored as

$$[A] = [R]^{-1}[\Lambda]\,[R] \tag{35}$$

where $[\Lambda]$ is the diagonal eigenvalue matrix of $[A]$ and $[R]$ is the corresponding eigenvector matrix of $[A]$. The complete form of the Jacobian matrix $[A]$ and the matrices $[R]$ and $[R]^{-1}$ are given in Ref. 16.

The matrix $[\,|A|\,]$ is defined as

$$[|A|] = [R]^{-1}[\,|\Lambda|\,]\,[R] \tag{36}$$

where $[\,|\Lambda|\,]$ is the diagonal absolute eigenvalue matrix of $[A]$. Matrix $[A]$ has six eigenvalues λ_i, and the minimum value for the eigenvalues λ_i is restricted according to Harten {Ref. 20} such that

$$|\lambda_i| = \begin{cases} |\lambda_i|, & |\lambda_i| > \epsilon_\lambda \\ 0.5\left(\dfrac{\lambda_i^2}{\epsilon_\lambda} + \epsilon_\lambda\right), & |\lambda_i| < \epsilon_\lambda \end{cases} \tag{37}$$

where ϵ_λ is the eigenvalue limiter.

The determination of the numerical viscous fluxes involves evaluation of the first derivatives of the components of velocity, the temperature, the turbulence kinetic energy, and the turbulence dissipation rate at the nodes. In the cell-centered scheme discussed above, the primitive variables are assumed to be piecewise constant. That is, they are assumed to be constant for an

element. In order to compute the first derivatives at the nodes, a bilinear variation of these primitive variables is assumed for quadrilateral elements, and a linear variation is assumed for triangular elements. Under these assumptions, the first derivative of a variable, T, for example, at any point in an element can be written as

$$\frac{\partial T}{\partial x} = [N]\left\{\frac{\partial T}{\partial x}\right\} \tag{38}$$

where $[N]$ are the shape functions and $\left\{\frac{\partial T}{\partial x}\right\}$ is the nodal first derivative vector of the element. By multiplying left-hand-side of Eqn. (38) by $\{N\}$ and on integration by parts we obtain

$$\int_{\Omega_e} \frac{\partial T}{\partial x}\{N\}d\Omega = \int_{\Gamma_e} nT\{N\}d\Gamma - \int_{\Omega_e} T\left\{\frac{\partial N}{\partial x}\right\} d\Omega \tag{39}$$

where n are the direction cosines. By multiplying the right-hand-side of Eqn. (38) by $\{N\}$ and on integration we obtain

$$\begin{aligned}\int_{\Omega_e} \{N\}[N]\left\{\frac{\partial T}{\partial x}\right\} d\Omega &= \int_{\Omega_e} \{N\}[N]d\Omega\left\{\frac{\partial T}{\partial x}\right\} \\ &= [M_L]\left\{\frac{\partial T}{\partial x}\right\}\end{aligned} \tag{40}$$

where $[M_L]$ is the lumped mass matrix obtained by diagonalizing the consistent mass matrix or the capacitance matrix. By substituting Eqn. (40) in Eqn. (39) and rearranging, we obtain the following expression:

$$\left\{\frac{\partial T}{\partial x}\right\} = \frac{1}{[M_L]}\left[\int_{\Gamma_e} nT\{N\}d\Gamma - \int_{\Omega_e} T\left\{\frac{\partial N}{\partial x}\right\}d\Omega\right] \tag{41}$$

To compute the first derivative at a particular node i, an assembly operation is performed where contributions from all the elements (ne) that have i as a common node are summed up. This operation results in the following relation for the first derivative at node i.

$$\frac{\partial T}{\partial x}_i = \frac{1}{[M_L]_i}\left[BT_{xi} - \sum_{e=1}^{ne} \int_{\Omega_e} T_e \left\{\frac{\partial N}{\partial x}\right\} d\Omega \right] \tag{42}$$

where $[M_L]_i$ is the coefficient of the global (assembled) lumped mass matrix for node i, BT_{xi} is the assembled boundary term (needs to be evaluated only at the domain boundary) surrounding node i, and T_e is the temperature of the element e.

The source terms in the turbulence equations are computed at the element level. The velocity derivatives needed at the element level to compute these source terms are obtained by averaging the nodal derivatives of the element. The cross-diffusion terms required for the k-ε model are also computed at the element level, similar to the source terms.

Point-Implicit Time Stepping Technique

Substituting Eqn. (33) for the inviscid numerical flux in Eqn. (32) and rearranging, we have

$$\{\Delta U_e\}^m = \frac{\Delta t}{\Omega_e}\{ -\frac{1}{2}\sum_{s=1}^{nside} \delta_s \left[\{F_R\}^{m+1} + \{F_L\}^{m+1} - [|A|]^{m+1}\left(\{U_R\}^{m+1} - \{U_L\}^{m+1}\right)\right]_s + \sum_{s=1}^{nside} \delta_s \{G_s\}^{m+1} + \Omega_e \{S_e\}^{m+1}\} \tag{43}$$

where $\{G_S\}$ represents the numerical viscous flux vector for the side s and the subscript e represents the element under consideration. The time integration scheme as shown above is a fully implicit technique and leads to solving the entire global system of equations. Equation (43) can be linearized by employing a Gauss-Seidel point relaxation scheme which results in a point-implicit scheme where the set of governing equations is solved at each element

as given in {Ref. 1}. The point-implicit scheme is represented in the following equation.

$$\left(I+\frac{\Delta t}{\Omega_e}\sum_{s=1}^{nside}\delta_s\left(\frac{1}{2}[|A|]^*-[B]^m\right)_s-\Delta t\left[\frac{\partial S}{\partial U}\right]^m\right)\{\Delta U_e\}^m =$$

$$\frac{\Delta t}{\Omega_e}\{-\frac{1}{2}\sum_{s=1}^{nside}\delta_s\left[\{F_R\}^*+\{F_L\}^m-[|A|]^*(\{U_R\}^*-\{U_L\}^m)\right]_s$$

$$+\sum_{s=1}^{nside}\delta_s[\{G_s\}^m]+\Omega_e\{S_e\}^m\} \qquad (44)$$

where superscript * refers to the latest available value. Matrix $[B_s]$ represents the implicit contribution from the viscous fluxes and the matrix $[\frac{\partial S}{\partial U}]$ denotes the Jacobian of the source terms in the governing equations for the turbulence variables.

LARCNESS Computations

This section describes the application of LARCNESS to the problems of shock-shock interferences in hypersonic flow. Comparison of laminar flow computations with that of turbulent flow are made wherever applicable. The turbulence models used in this work do not predict transition and in all the applications discussed in this section, no account was made for the transition from laminar to turbulent flow. For the application problems, an initial solution is obtained without the source terms in the turbulence governing equations and these terms are introduced later into the equations to obtain a final converged solution. The freestream turbulent viscosity is always assumed to be of the same order of magnitude as the freestream laminar viscosity and the freestream turbulent kinetic energy is assumed to be 0.1% of the freestream mean flow kinetic energy. The validation of the code was performed by two test cases and the results are presented in {Ref. 9}.

The computer program for the solution algorithm is fully vectorized on the CRAY computers and requires a memory of 11.8 MW for the turbulent flow

computations on a 200,000 element mesh compared to 9.4 MW of memory for laminar computations on the same mesh. On a CRAY-C90 computer, LARCNESS code took 8.44E-06 CPU seconds/element/iteration for laminar flow computations (for a 35,000 element mesh) compared to 1.07E-05 CPU seconds/element/iteration for the turbulent computations on the same mesh. It is interesting to note that the increase in the CPU time for the turbulent calculations is only 20% more than that for the laminar calculations.

Type IV Shock-Shock Interference in a Mach 11 Flow

The wall pressure and heat flux amplification is a maximum for the Type IV shock-shock interference relative to the rest of the interferences as mentioned in Ref. 21. A schematic of the Type IV interference is shown in Fig. 1. In a typical Type IV interference, the impinging shock interferes with the near normal portion of the bow shock resulting in a supersonic jet that impinges on the body. This supersonic jet terminates through a normal shock before it reaches the body, creating a small stagnation region where the heat fluxes are the maximum. The supersonic jet is surrounded by shear layers, the nature of which (either laminar or turbulent) plays a role in augmenting the wall heat fluxes {Ref. 22}. To investigate the effects of turbulence this problem was run with both the laminar and turbulent options under two sets of freestream conditions as given in Table A. These freestream conditions are for air which is considered as a perfect gas with ratio of specific heats, γ, of 1.4. The first set of conditions, referred to as condition A (throughout this report), is at a freestream Mach number of 11.36 and freestream Reynolds number of 6500 based on the cylinder radius, and is assumed to correspond to laminar shear layer flow conditions. The second set, referred to as condition B (throughout this report), is at a freestream Mach number of 11.03 and freestream Reynolds number of

414,000 and is assumed to correspond to turbulent shear layer flow conditions. These freestream condition sets correspond to experimental test conditions to be reported at a later date by R.J. Nowak***. For both the sets of freestream conditions, the wall temperature was fixed at 530°R. Since the freestream conditions played a major role in the computations, results from LARCNESS computations are presented in two separate subsections for the two condition sets in the following discussion.

Freestream condition set A

This set of freestream conditions corresponds to a lower Reynolds number as mentioned above. Before the shock-shock interference problem was attempted, an undisturbed flow (without the shock-shock interference) under the same conditions over a 1.5 inch radius cylinder as shown in Fig. 2 (problem statement) was analyzed using the LARCNESS code. The theoretical stagnation heat flux, q_o, was computed from the Fay and Riddel theory {Ref. 23} for the undisturbed flow without the shock-shock interference . The wall heat flux distribution q from the LARCNESS computations non-dimensionalized with respect to the theoretical stagnation heat flux q_o is shown in Fig. 3. The computational stagnation heat flux was within 2% of the theoretical stagnation heat flux.

For the shock-shock interference flow problem as shown in Fig. 4, successive mesh adaptation was performed until the last two meshes essentially gave the same result. These meshes consisted of: (a) highly stretched structured grids next to the wall, and (b) solution adapted unstructured grids everywhere else. The unstructured portion of the mesh adaptation was accomplished by a combination of three different adaptive techniques. The first

*** Dr. R.J. Nowak can be reached at NASA LaRC by phone at (804) 864-1341 or by mail at M/S 408A

technique is the adaptive remeshing where a new mesh is created based on the solution from a previous mesh {Ref. 24}. The adaptive remeshing did not produce the level of refinement that was required in the shear layers. Therefore the second technique of subdividing the elements in the shear layer region was employed in association with the remeshing technique. To further enhance the quality of the mesh, a third technique known as adaptive mesh movement was used where the nodes in the mesh are moved closer to each other wherever higher levels of mesh refinement was desired. This combination of mesh refinement techniques applied to high speed flows is described in {Refs. 9 & 25}. The final mesh consisted of 210,195 elements and 119,959 nodes. The size of the smallest element was $4X10^{-7}$ inches. A portion of this final mesh near the stagnation region is shown in Fig. 5. Convergence criterion was set at 3 or 4 orders of magnitude reduction in all the residuals corresponding to the mean flow variables and less than 1% change in the peak heat flux value over a specified period of time (at least 1000 iterations). The convergence in terms of peak heat flux history for the last 3000 time iterations on the final mesh for condition set A under laminar flow conditions is shows in Fig. 6. Table B includes the coordinates of the two triple points and the transmitted shock lengths for both the laminar and turbulent cases corresponding to freestream condition set A.

The total velocity contours, pressure contours, and first derivative of density contours near the stagnation region, from the LARCNESS computations on the final mesh, are shown in Fig. 7, 8, and 9. The x and y axes shown in these figures are reference axes parallel to the coordinate axes X and Y (the origin of these reference axes is not shown at the center of the cylinder which is the origin for the coordinate axes). These contours show the intricate details of the flow field the shear layers, the supersonic jet and the jet terminating shock.

The jet terminating shock location as shown in these contour plots suggests that this case does not represent the peak Type IV case where the jet terminating shock is parallel to the cylinder wall and hence the supersonic jet impingement is normal to the wall. Turbulent flow computations were performed using the LARCNESS code and the total velocity contours near the stagnation region from both the laminar and the turbulent computation are compared in Fig. 10. The shear layers in the turbulent case appear to be thicker than that of the laminar case. The wall heat flux distribution from the turbulent computations was compared with that of laminar computations and is shown in Fig 11A. Although there was a shift in the location of the peak heat flux (about 2^{o}), there was no significant difference between the magnitudes of the peak heat flux in both the cases. The reason that the wall heat flux distributions are not very different from each other is that the freestream Reynolds number is very small and the influence of the turbulence effects on the flow field are negligible. Similarly the wall pressure distributions from the laminar and the turbulent computations is shown in Fig 11b. A trend similar to that of the wall heat flux distributions was observed for the wall pressure distributions. To investigate the influence of the impinging shock location in the inlet plane of the computational domain, the original location of the impinging shock was lowered by 0.055 inches and laminar computations were performed for this new impinging shock location. The comparisons of the wall heat flux distributions and the wall pressure distributions from the laminar computations for the two impinging shock locations are shown in Fig. 12. For this freestream condition set, although there was a difference in the locations of the peaks in terms of wall pressures and wall heat fluxes as expected, there were no major differences in the magnitudes of these two quantities for the two impinging shock locations. Table C contains the location of the peaks and values of these peaks (in terms

of degrees) of wall pressures and wall heat fluxes for both laminar and turbulent cases for this freestream condition set A. The magnitudes of the peak pressure in Table C are non-dimensionalized with respect to p_o, the theoretical stagnation pressure of 0.5159 psia. The magnitudes of the peak heat flux in the table are non-dimensionalized with respect to q_o, the theoretical stagnation heat flux of 20.26 Btu/ft^2-sec.

Freestream condition set B

This freestream condition set corresponds to a higher Reynolds number and is assumed to be under turbulent shear layer conditions. To understand the effects of turbulence on the flow field, this case was run under laminar as well as turbulent conditions. The most refined mesh for the turbulent case consisted of 245,873 elements and 156,432 nodes. The size of the smallest element next to the wall in the normal direction is 4×10^{-8} inches. A similar level of refinement was obtained on the mesh for the laminar case. The convergence criterion was the same as that mentioned in the discussion under freestream condition set A. The contours of pressure, and the first derivative of density are shown in Figs. 13, 14. Again in these contour plots, the axes x and y represent the reference axes only and their origin is not at the center of the cylinder. Figure 15a show the total velocity contours in the entire flow field. Figure 15b shows the total velocity contours near the stagnation region for the laminar case and Fig. 15c shows the total velocity contours for the turbulent case. One may observe from this figures 15b and 15c that the turbulent shear layers are thicker than the laminar shear layers. To obtain an estimate of the shear layer growth and thickness, a normal cut parallel to the y-axis was made through the shear layer in the region between the 1st and the 2nd triple points (see Figure 1 and 4). The shear layer thickness at a given x-location is defined as the y-distance between the upper and lower points in the shear layer where u-velocities are

97.5% of the upper and lower local freestream velocities respectively. At x = -2.076 inches from the center of the cylinder, the shear layer thickness for the turbulent case was 0.3134 inch; and the shear layer thickness for the laminar case was 0.2663 inch (about 15% thinner). However, the shock-shock structure including the triple points was farther from the body for the turbulent case compared to the laminar case. In order to compare laminar and turbulent shear layer thickness at the same distance from the respective 1st triple points, the laminar shear layer thickness was calculated at x = -1.973 inches, which is the distance from the 1st triple point for the above turbulent shear layer thickness. The shear layer thickness for the laminar case at this location was 0.2015 inches which is significantly thinner (about 67%) than the turbulent case. Similar to the case of freestream condition set A, the jet terminating shock is not parallel to the wall indicating that this case does not represent the peak Type IV location. Therefore, the shear layer effects on the stagnation region are predominant. Fig. 16 shows the streamline contours superimposed on the total velocity contours for the turbulent case. These contours show that a major portion of the flow going towards the stagnation point is coming from the supersonic jet region and the upper shear layer.

The wall heat flux distributions from the laminar and turbulent computations are shown in Fig. 17a. The peak heat flux distribution from the turbulent computations is significantly higher than peak heat flux from the laminar computations. The location of the peak in the turbulent computations is also different from the laminar computations and this difference is again attributed to the shift in the shock structure as explained above. The comparison of the wall pressure distributions for the laminar and the turbulent cases is shown in Fig. 17b. The peak pressure in the turbulent case seems to be lower than that of the laminar case. Two different sets of computations were

performed for two different impinging shock locations. Fig. 18 shows the comparison of the wall heat flux distributions and the wall pressure distributions for the two impinging shock locations and there is a clear evidence of high sensitivity of the peak pressure and peak heat flux to the location of the incoming impinging shock. Table E contains the location of the peaks (in terms of degrees) of wall pressures and wall heat fluxes for both the cases for this freestream condition set B. The magnitudes of the peak pressure in Table E are non-dimensionalized with respect to p_o, the theoretical stagnation pressure of 7.005 psia. The magnitudes of the peak heat flux in the table are non-dimensionalized with respect to q_o, the theoretical stagnation heat flux of 19.78 Btu/ft^2-sec.

Concluding Remarks

A two-equation compressible turbulence model is implemented in a point-implicit, cell-centered , upwind algorithm applicable to unstructured grids. The current turbulence model based on a zonal approach involves k, the turbulent kinetic energy and ω, the specific turbulence dissipation rate as the two turbulence variables. This model results in the standard k-ω model in the boundary layer next to the wall and results in the standard k-ε model away from the wall by inclusion of a cross-diffusion term in the governing equation for the specific dissipation rate. The governing equations for the turbulence variables are solved simultaneously with the equations governing the mean flow. For the problem of a 2-D hypersonic flow (Mach 11) over a circular cylinder, the peak heat flux from the laminar flow computations agreed well with the peak heat flux computed from the Fay and Riddel theory.

For the Type IV shock-shock interference in a hypersonic flow over a cylinder, two sets of freestream conditions were chosen with two different

freestream Reynolds numbers. The flow conditions at the higher Reynolds number freestream conditions are assumed to be turbulent. For the first set of freestream conditions, the results from the laminar and turbulent computations did not differ significantly from each other. Highly refined solution adaptive meshes were used in these computations to capture the intricate flow details such as the shear layers, the supersonic jet, and the jet terminating shock. The sensitivity of the augmented pressures and heat fluxes due to the variation in the location of the incoming impinging shock seem to be less significant for this freestream condition set.

For the second set of freestream conditions with a higher freestream Reynolds number, there were significant differences in the results from the laminar and turbulent conditions. The velocity contours showed thicker shear layers in the turbulent computations relative to that of laminar computations. The wall heat flux distribution from the turbulent computations showed a 40% increase in the value of the peak heat flux compared to that of laminar computations. The peak wall pressure in the turbulent computations was lower relative to the peak in the laminar computations.

The current work is one of the first attempts to apply two-equation turbulence models to the shock-shock interference problem. As the freestream Reynolds number goes higher, the turbulence effects seem to influence the flow field stronger and result in higher wall peak heat fluxes and wall peak pressures.

Acknowledgments

The author would like to thank Dr. Robert Nowak from NASA LaRC, Dr. Johnny Narayan from Arizona State University, and Mr. Joseph Morrison from AS&M for the technical information and discussions. The technical suggestions given by Dr. Florian R. Menter of Eloret Institute and Dr. David Wilcox of DCW

Industries are gratefully acknowledged. This work is dedicated to the author's friend and former colleague, Dr. Pramote Dechaumpai.

References

1. Thareja, R.R., Stewart, J.R., Hassan, O., Morgan, K. and Peraire, J., "A Point Implicit Unstructured Grid Solver for the Euler and Navier-Stokes Equations", *International Journal for Numerical Methods in Fluids*, Vol. 9, 1989, pp. 405-425, also AIAA 88-0036.

2. Wieting, A.R., and Holden, M.S., "Experimental Study of Shock Wave Interference Heating on a Cylindrical Leading Edge", *AIAA Journal*, Vol. 27, No. 11, 1989, pp. 1557-1565.

3. Baldwin, B.S., and Lomax J., "Thin Layer Approximation and Algebraic Model for Separated Turbulent Flows", AIAA 78-275, January 1978.

4. Jones, W.P., and Launder, B.E., "The Calculation of Low-Reynolds Number Phenomena with a Two-Equation Model of Turbulence", *International Journal of Heat and Mass Transfer*, Vol. 16, 1973, pp. 1119-1130.

5. Speziale, C.G., Abid, R., and Anderson, E.C., "A Critical Evaluation of Two-Equation Models for Near Wall Turbulence", ICASE Report 90-46, also NASA CR 182068, AIAA 90-1481, June 1990.

6. Patel, V.C., Rodi, W., and Scheuerer, G., "Turbulence Models for Near-Wall and Low Reynolds Number Flows: A Review", *AIAA Journal*, Vol. 23, 1985, pp. 1308-1319.

7. Lang, N.J., and Shih, H., "A Critical Comparison of Two-Equation Turbulence Models", NASA Technical Memorandum 105237, September 1991.

8. Zhang, H.S., So, R.M.C., Speziale, C.G., and Lai, Y.G., "A Near-Wall Two-Equation Model for Compressible Turbulent Flows", AIAA 92-0442, January 1992.

9. Vemaganti, G.R., and Prabhu, R.K., "Application of a Two-Equation Turbulence Model for High Speed Compressible Flows Using Unstructured Grids", AIAA 93-3029, July 1993.

10. Menter, F.R., "Performance of Popular Turbulence Models for Attached and Separated Adverse Pressure Gradient Flows", AIAA Journal, Vol. 30, No. 8, August 1992, pp. 2066-2072.

11. Menter, F.R., "Zonal Two Equation k-ω Turbulence Models for Aerodynamic Flows", AIAA 93-2906, July 1993.

12. Wilcox, D.C., "Turbulence and Transition Modeling for High Speed Flows", NASA Contractor Report 191473, April 1993.

13. Wilcox, D.C., "A Two-Equation Turbulence Model for Wall-Bounded and Free-Shear Flows", AIAA 93-2905, July 1993.

14. Marcum, D.L., and Agarwal, R.K., "A Three-Dimensional Finite Element Navier-Stokes Solver with k-e Turbulence Model for Unstructured Grids", AIAA 90-1652, June 1990.

15. Mavriplis, D.J., and Martinelli, L., "Multigrid Solution of Compressible Turbulent Flow on Unstructured Meshes Using a Two-Equation Model", AIAA 91-0237, January 1991.

16. Morrison, J., "Flux Difference Split Scheme for Turbulent Transport Equations", AIAA 90-5251, October 1990.

17. Lang, N.J., and Shih, T.H., "A Critical Comparison of Two-Equation Turbulence Models", NASA Technical Memorandum 105237, September 1991.

18. Gnoffo, P.A.: " Application of Program Laura to Three-Dimensional AOTV Flow fields", AIAA 86-0565, January 1986.

19. Roe, P.L.: "Approximate Riemann Solvers, Parameter Vectors and Difference Scheme", *Journal of Computational Physics*, Vol. 43, 1981, pp. 357-372.

20. Harten, A. "High Resolution for Hyperbolic Conservation Laws", *Journal of Computational Physics*, Vol. 49, 1983, pp. 357-393.

21. Edney, B.: "Anomalous Heat Transfer and Pressure Distributions on Blunt Bodies at Hypersonic speeds in the Presence of an Impinging Shock", FFA Rep. 115, Aeronaut. Res. Inst. of Sweden, 1968.

22. Wieting, A.R.: "Multiple Shock-Shock Interference on a Cylindrical Leading Edge", AIAA 91-1800, June 1991.

23. Fay, J.A., and Riddel, F.R., "Theory of Stagnation Point Heat Transfer in Dissociated Air", *Journal of the Aeronautical Sciences*, Vol. 25, No. 2, February 1958, pp. 73-85,121.

24. Peraire, J., Vahdati, M., Morgan, K. and Zienkiewicz, O.C.: "Adaptive Remeshing for Compressible Flow Computations", *Journal of Computational Physics*, Vol 72, No. 2, 1987, pp.449-466.

25. Prabhu, R.K.: "An Implementation of a Chemical and Thermal Nonequilibrium Flow Solver on Unstructured Meshes and Application to Blunt Bodies", NASA Contractor Report 194967, August 1994.

Table A. Freestream conditions used for the Type IV interference analysis

Variable	freestream condition set A	freestream condition set B
Velocity	8366.87 ft/sec	5018.3 ft/sec
Mach no.	11.36	11.03
Reynolds no.	6636	413,974
Static Temperature	225.8°R	83.20°R
Static Pressure	3.051E-03 psia	4.396E-02 psia

** Freestream Reynolds number is based on the cylinder radius of 38.1 mm (1.5 in)

*** Flow conditions below the oblique shock were determined based on oblique shock relations with a flow deflection angle of 10° and a shock angle of 14.05°

Table B. Coordinates of the triple points and transmitted shock lengths for freestream condition set A for the impinging shock location 2

Case	1st triple point coords. (non-dim)	2nd triple point coords. (non-dim)	Transmitted shock length, in.
1) Laminar	x = -1.72069 y = -0.23732	x = -1.10384 y = -0.53386	1.02664
2) Turbulent	x = -1.70228 y = -0.22691	x = -1.11194 y = -0.51852	0.98765

*** All the coordinates are non-dimensionalized with respect to the cylinder radius of 38.10 mm (1.5 in)

Table C. Locations and magnitudes of the pressure and heat flux peaks for freestream condition set A

Case	Location of the pr. peak (deg)	Magnitude of the pr. peak	Location of the h.f. peak (deg)	Magnitude of the h.f. peak
1) Laminar (Impinging shock loc.1)	-32.00	17.00	-31.63	23.22
2) Laminar (Impinging shock loc.2)	-29.80	16.59	-29.60	23.60
3) Turbulent (Impinging shock loc.2)	-28.55	15.34	-28.26	21.67

*** The magnitudes of the pressure peaks are non-dimensionalized with respect to the stagnation pressure of 0.5159 psia. and the magnitudes of heat flux peaks are non-dimensionalized with respect to the stagnation heat flux of 20.26 Btu/ft^2-sec

Table D. Coordinates of the triple points and transmitted shock lengths for freestream condition set B for the impinging shock location 2

Case	1st triple point coords. (non-dim)	2nd triple point coords. (non-dim)	Transmitted shock length, mm.
1) Laminar	x = -1.70352 y = -0.24194	x = -1.08102 y = -0.54639	1.03944
2) Turbulent	x = -1.77225 y = -0.25909	x = -1.11177 y = -0.57525	1.09837

*** All the coordinates are non-dimensionalized with respect to the cylinder radius of 38.10 mm (1.5 in)

Table E. Locations and magnitudes of the pressure and heat flux peaks for freestream condition set B

Case	Location of the pr. peak (deg)	Magnitude of the pr. peak	Location of the h.f. peak (deg)	Magnitude of the h.f. peak
1) Laminar (Impinging shock loc.1)	-34.26	17.70	-33.76	24.63
2) Laminar (Impinging shock loc.2)	-30.14	15.96	-29.51	29.37
3) Turbulent (Impinging shock loc.1)	-32.12	11.18	-37.31	33.15
4) Turbulent (Impinging shock loc.2)	-32.53	12.67	-32.45	49.41

*** The magnitudes of the pressure peaks are non-dimensionalized with respect to the stagnation pressure for the undisturbed flow of 7.005 psia, and the magnitudes of the heat flux peaks are non-dimensionalized with respect to stagnation heat flux of 19.78 Btu/ft^2-sec

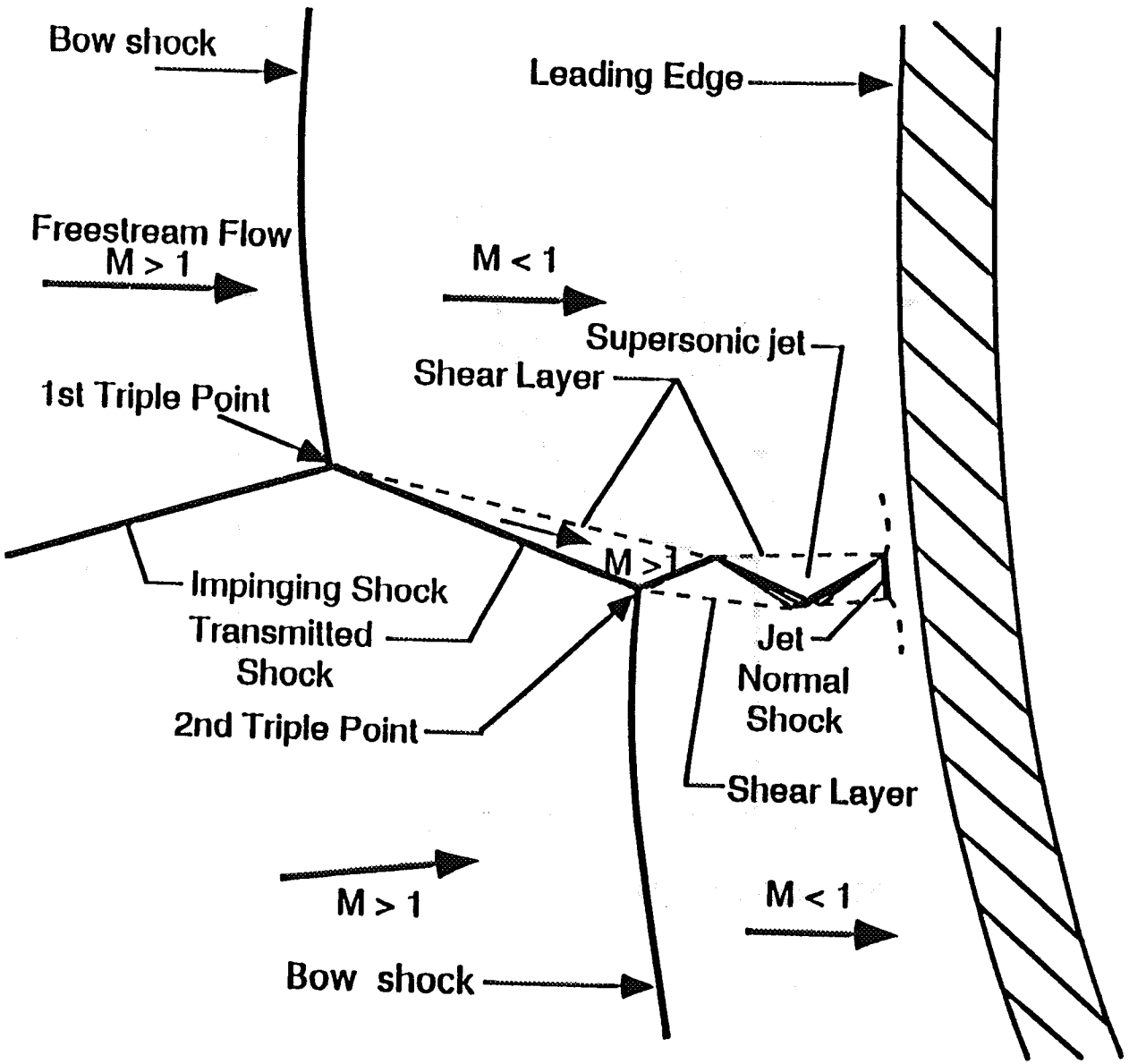

Fig.1 Details of the flow field in a Type IV shock-shock interefernce

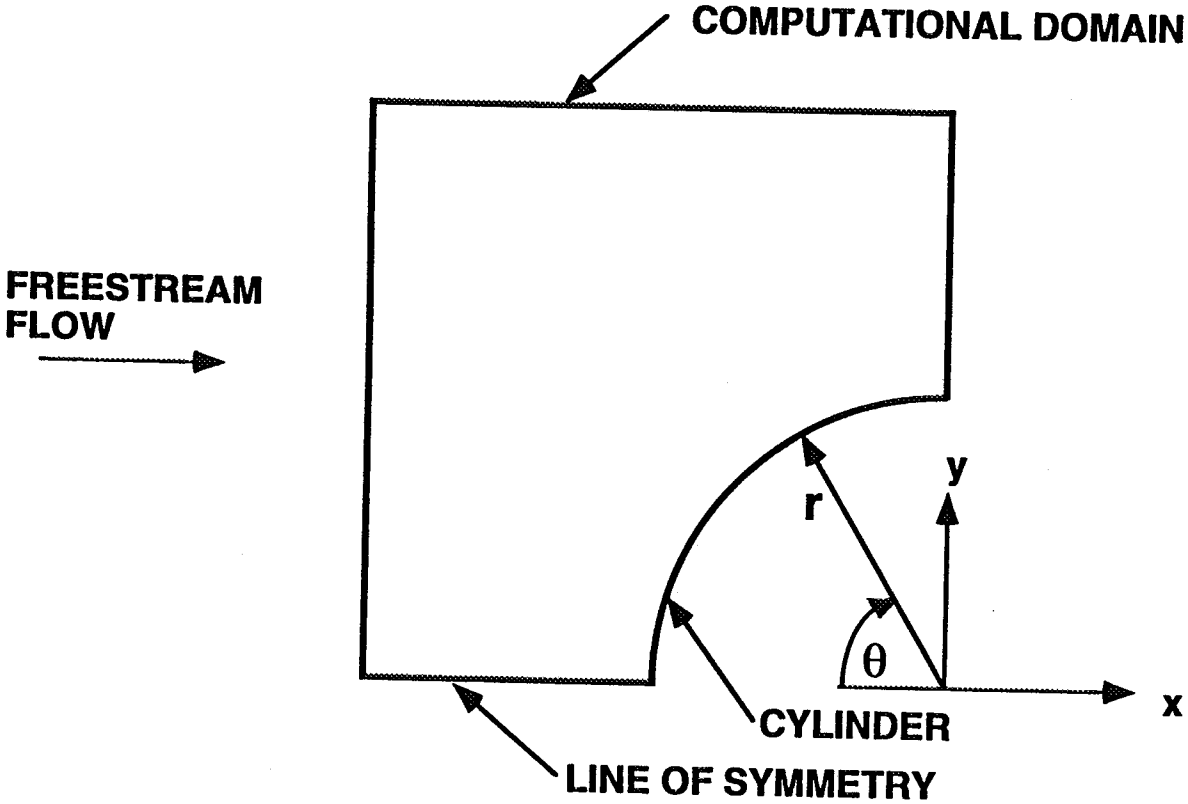

Fig.2 Problem statement for a hypersonic flow over a cylinder

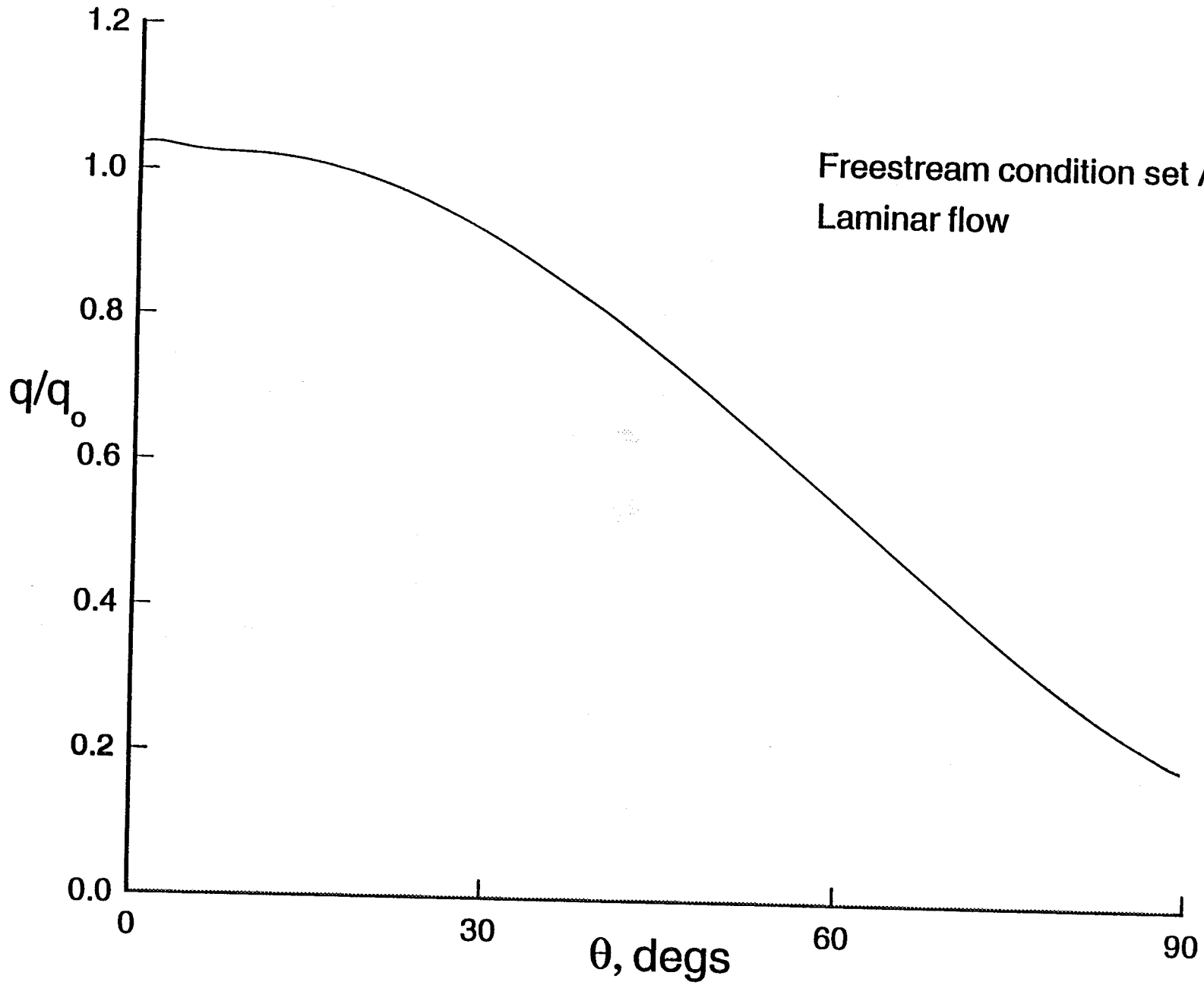

Fig.3 Wall heat flux distribution from LARCNESS computations for a laminar flow over a cylinder

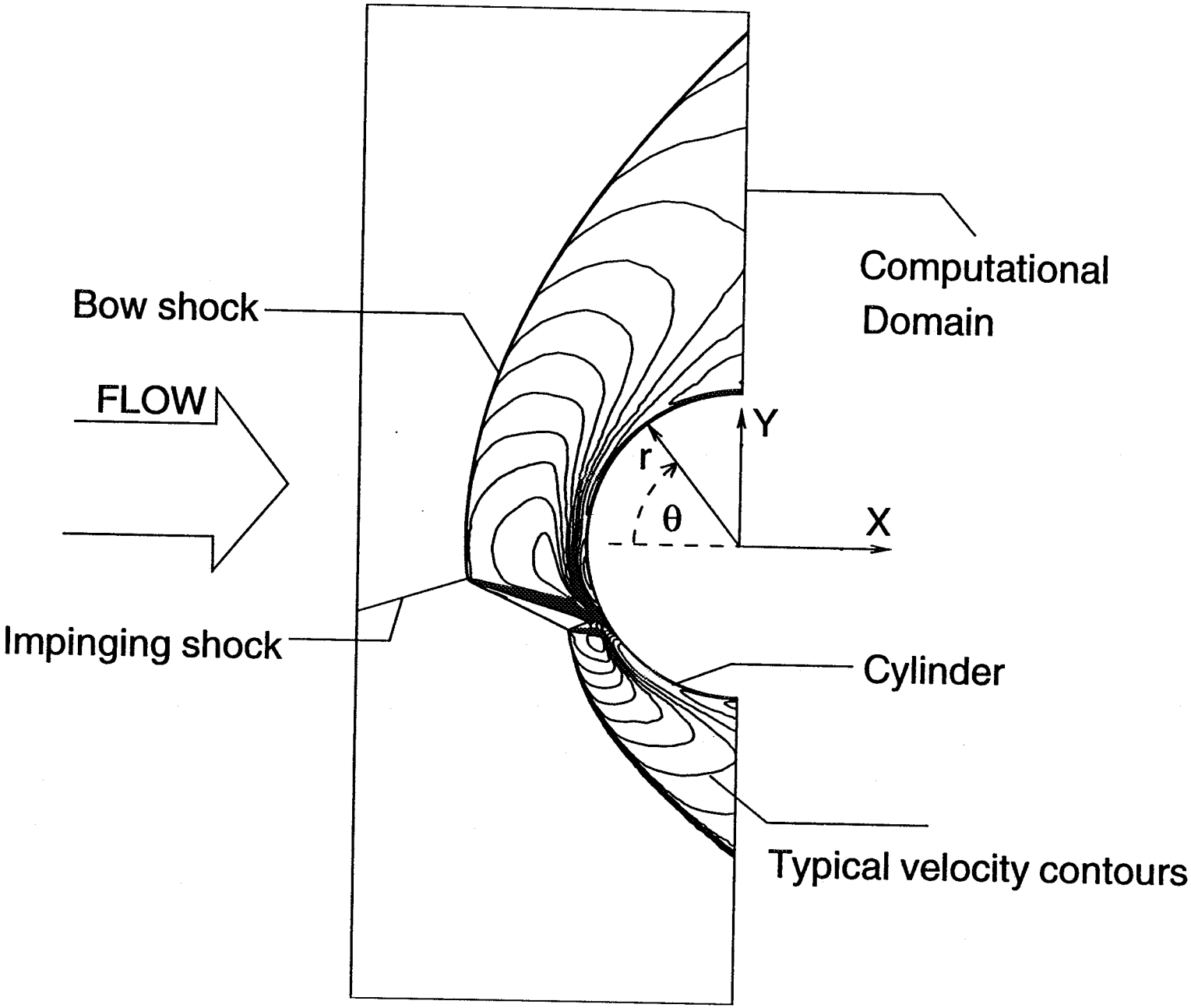

Fig.4 Problem statement for a Type IV shock-shock interference in a hypersonic flow

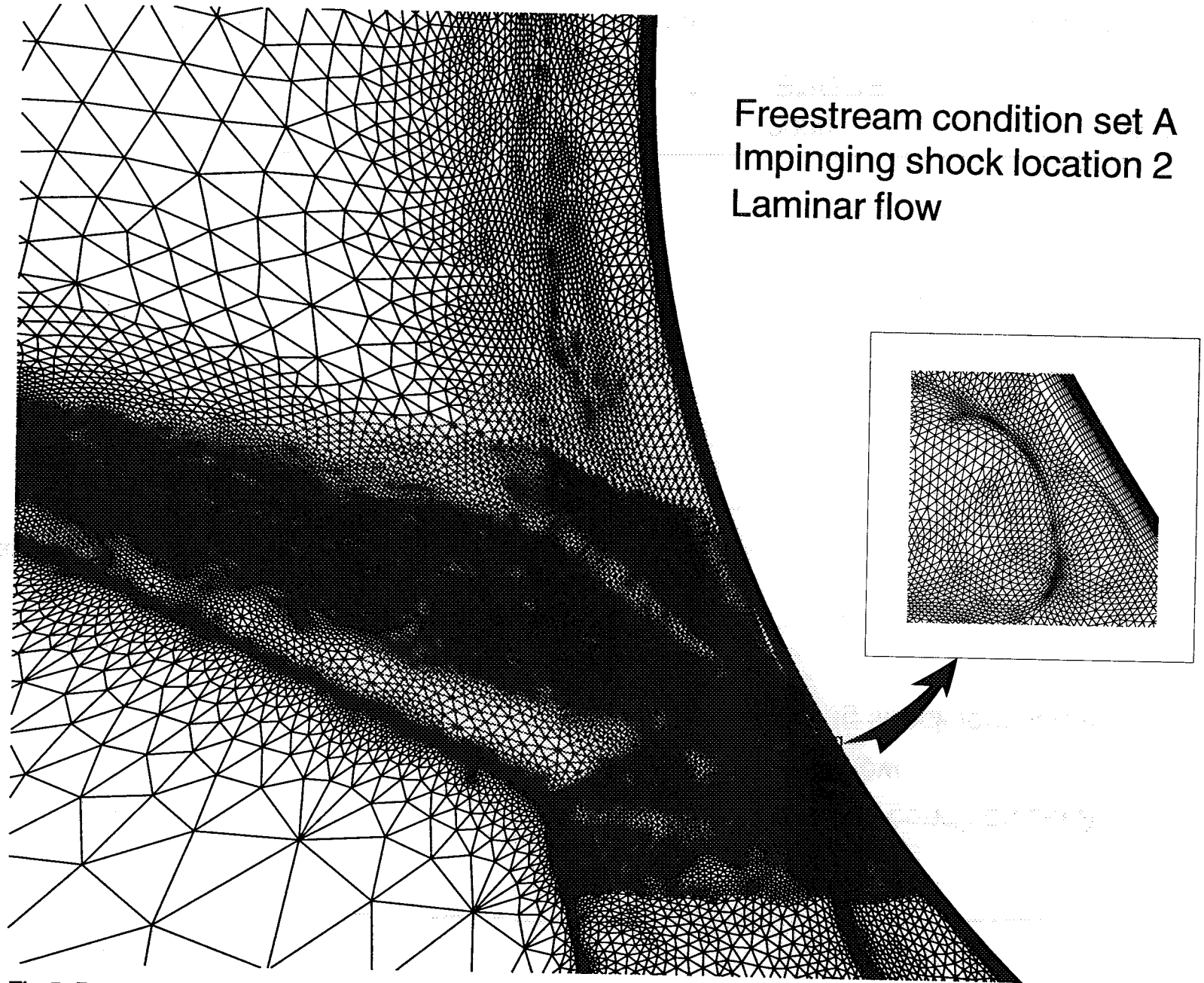

Fig.5 Details of the adapted mesh near the stagnation region of a Type IV shock interference

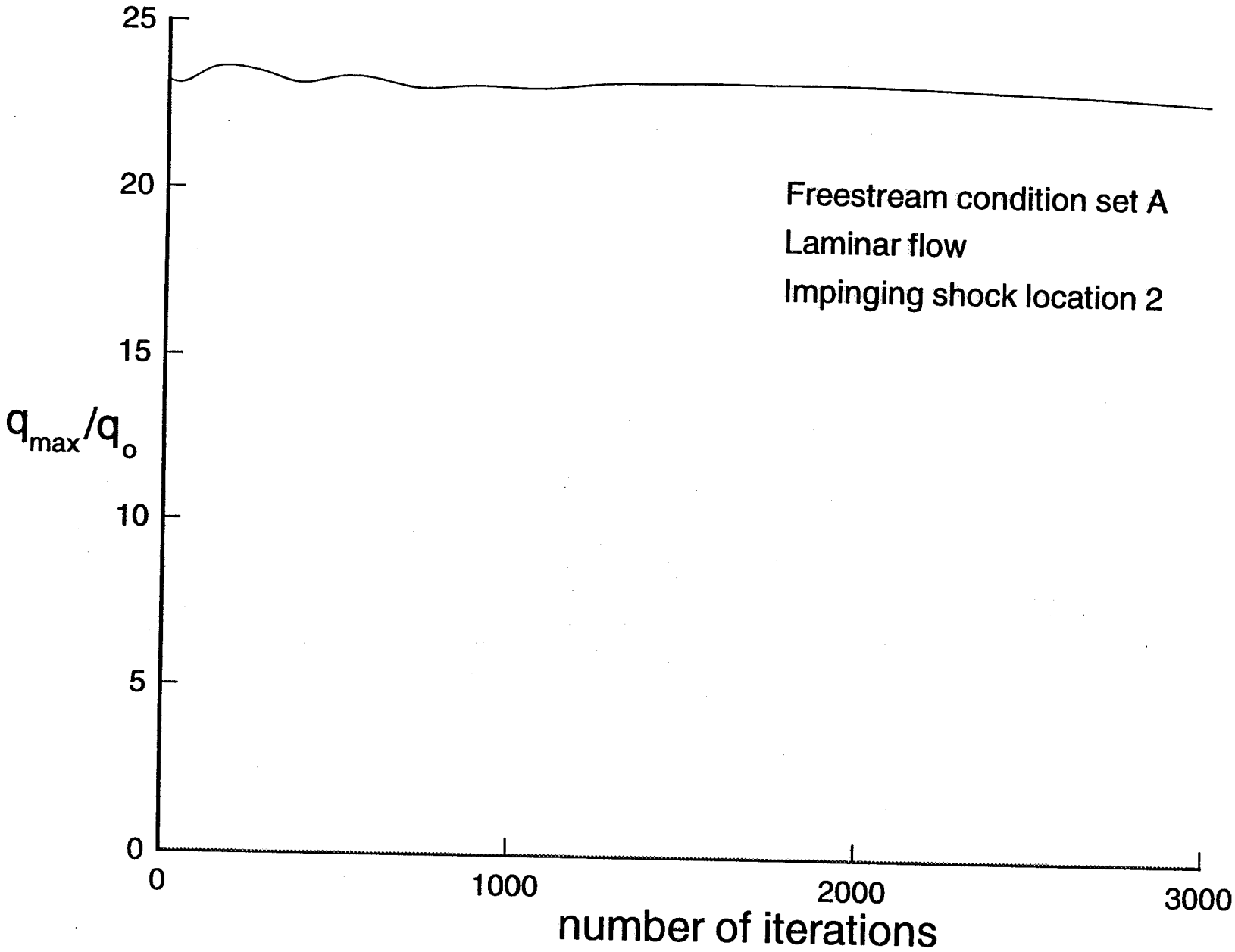

Fig.6 Convergence history of the peak heat flux for the Type IV shock interference

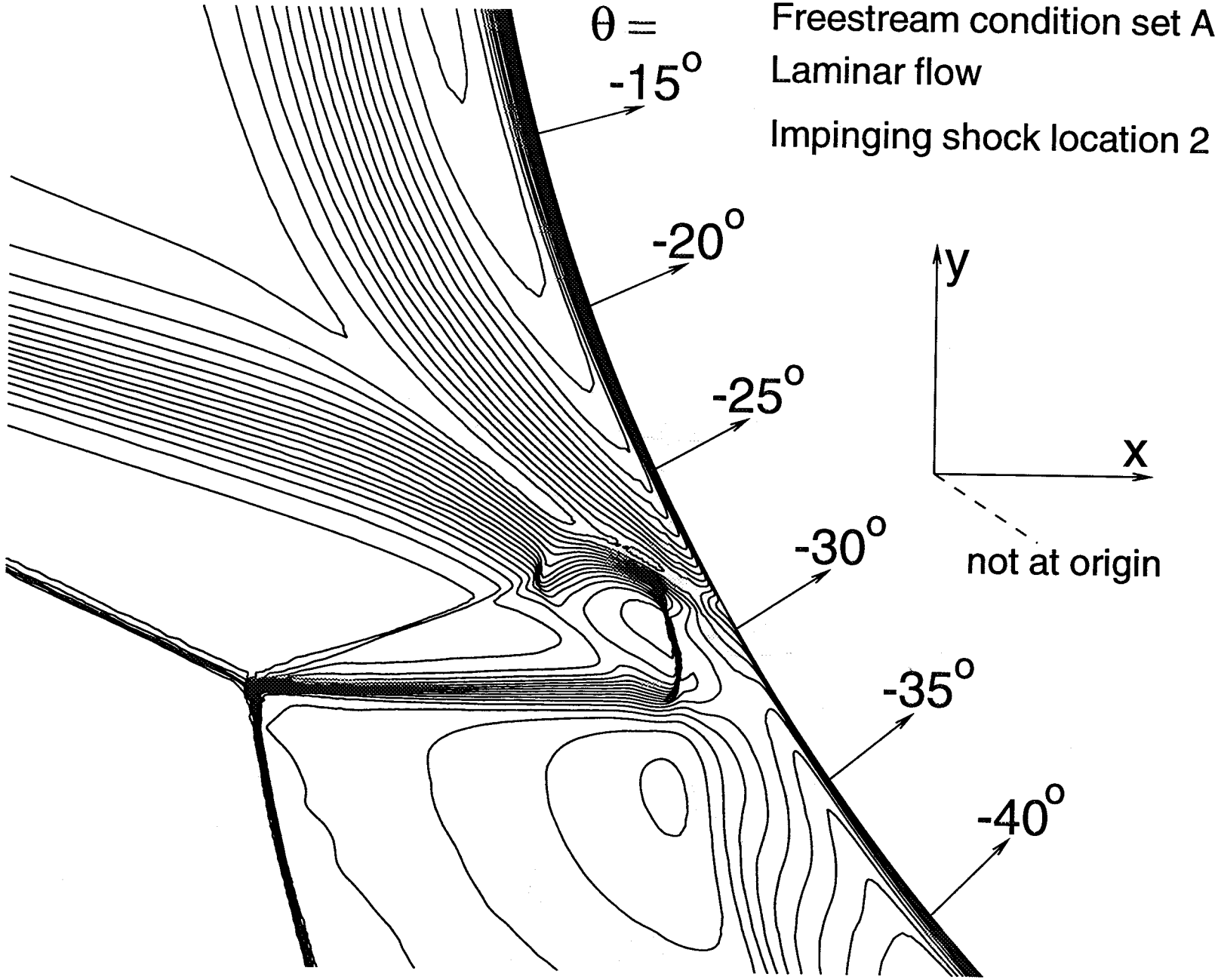

Fig.7 Total velocity contours near the stagnation region from the laminar computations for the Type IV interference at a freestream Reynolds number of 6,500

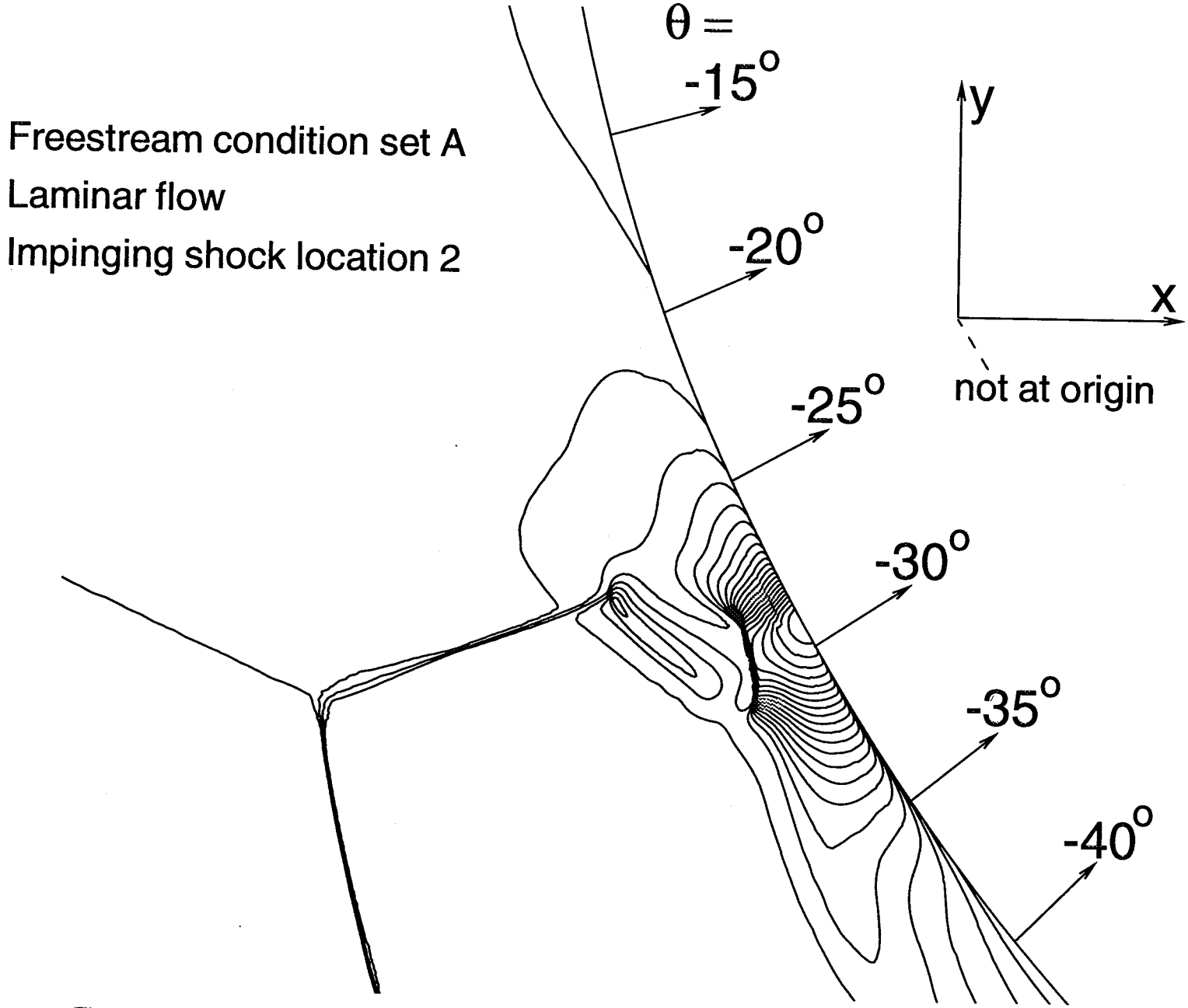

Fig.8 Pressure contours near the stagnation region from the laminar computations for the Type IV interference at a freestream Reynolds number of 6,500

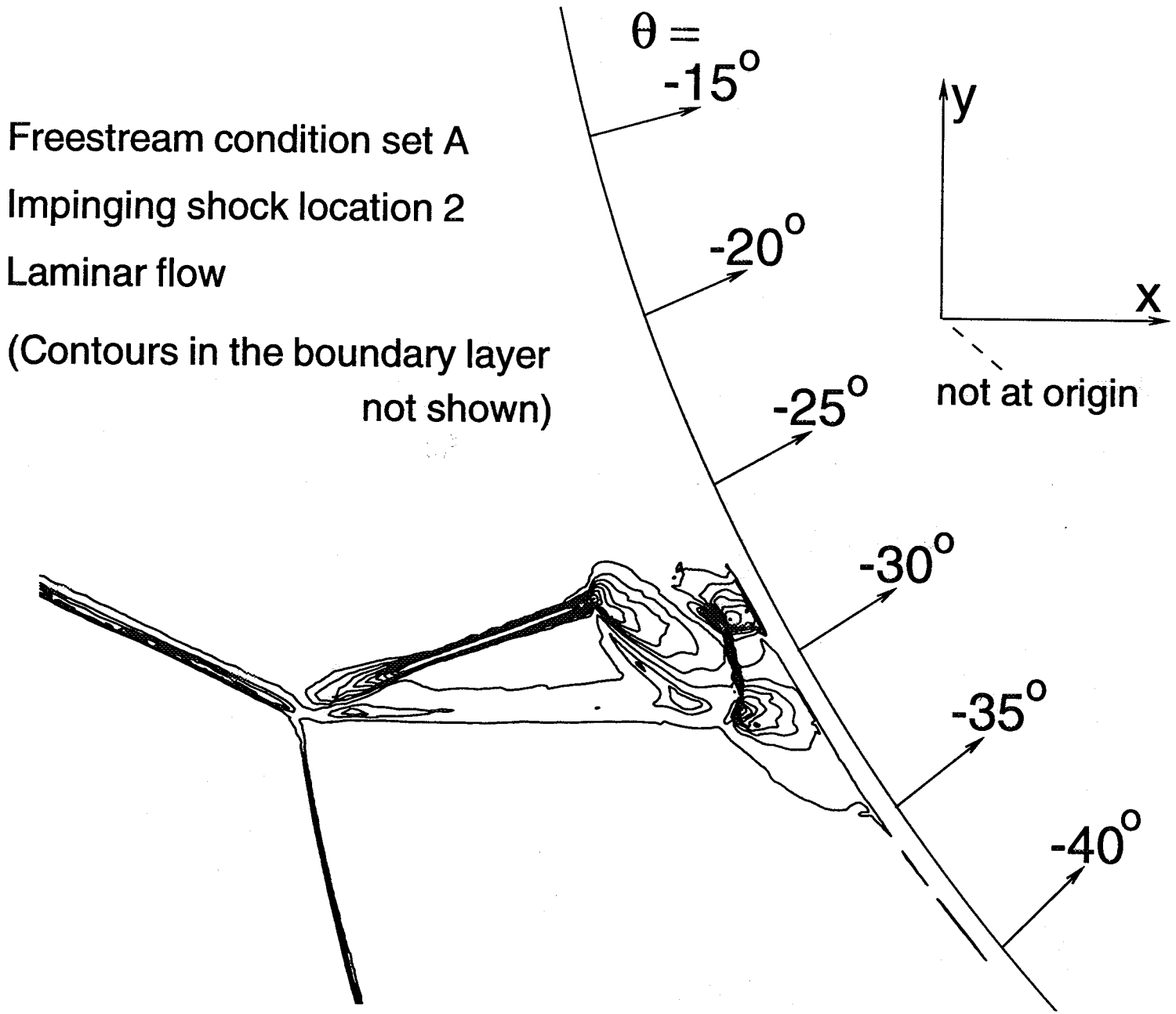

Fig.9 First derivative of density contours near the stagnation region from the LARCNESS computations for the Type IV interference at a freestream Reynolds number of 6,500

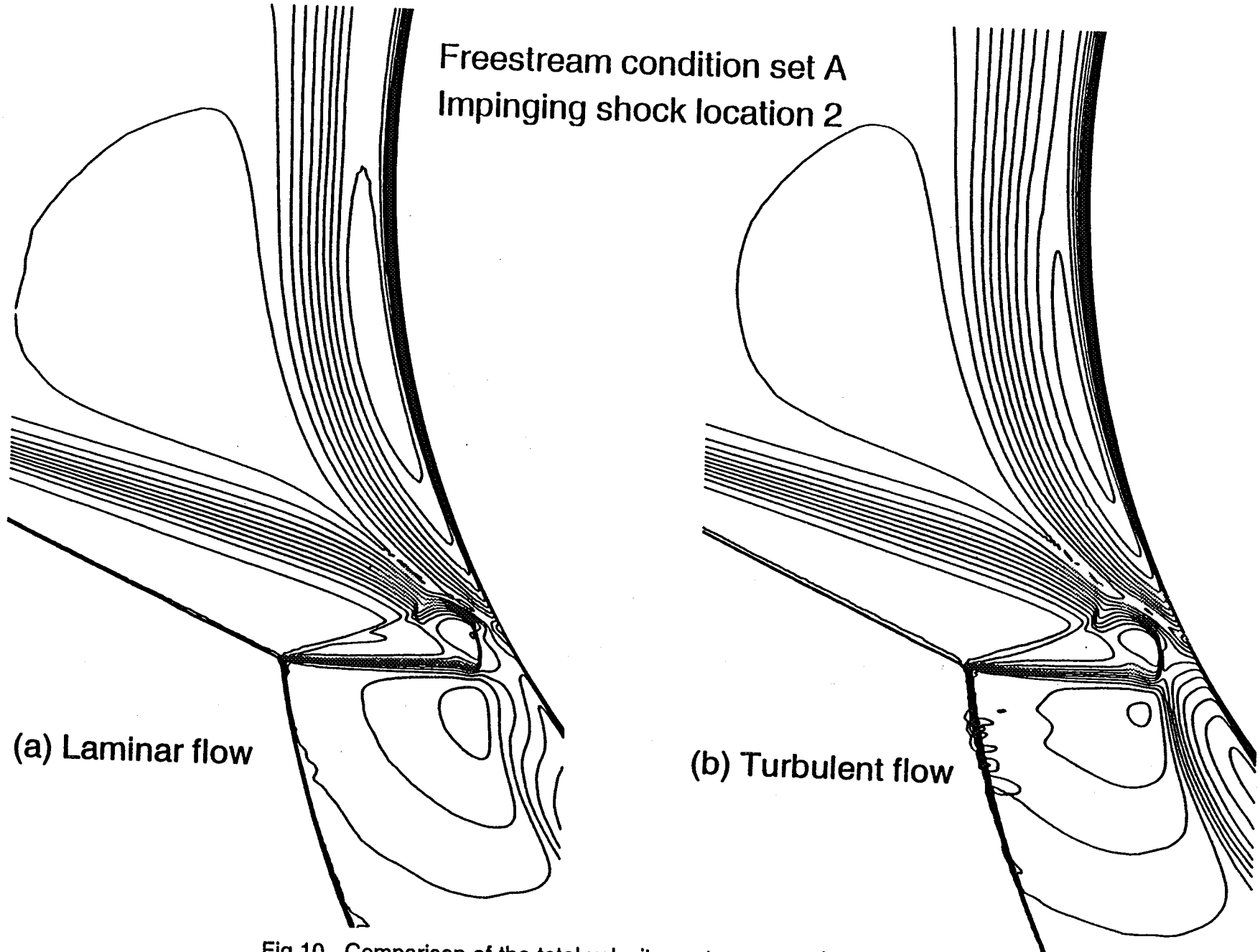

Fig.10 Comparison of the total velocity contours near the stagnation region from laminar and turbulent flow computations of Type IV interference at a freestream Reynolds number of 6,500

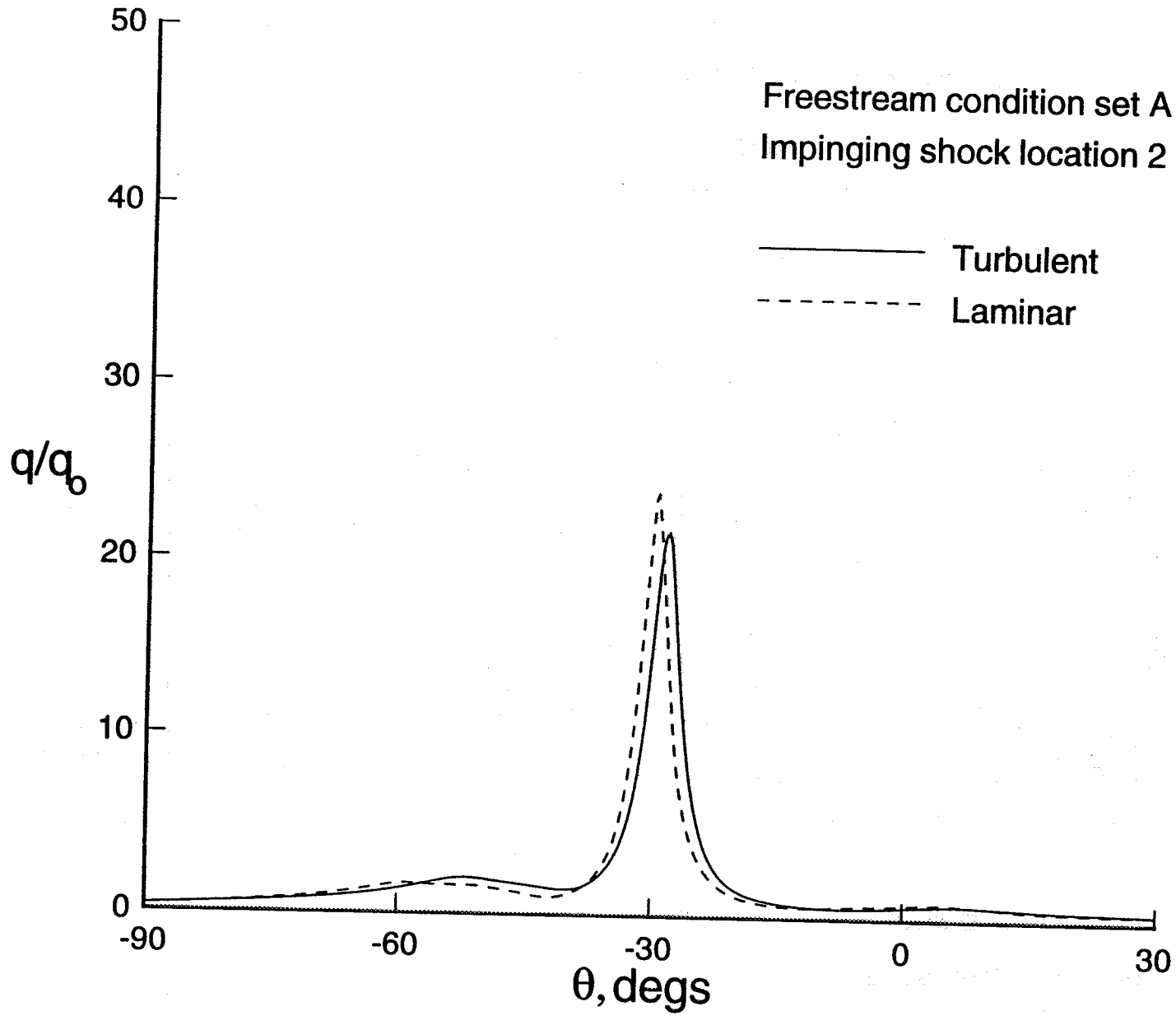

Fig.11a Comparison of the wall heat flux distributions from Type IV interference computations at a freestream Reynolds number of 6,500

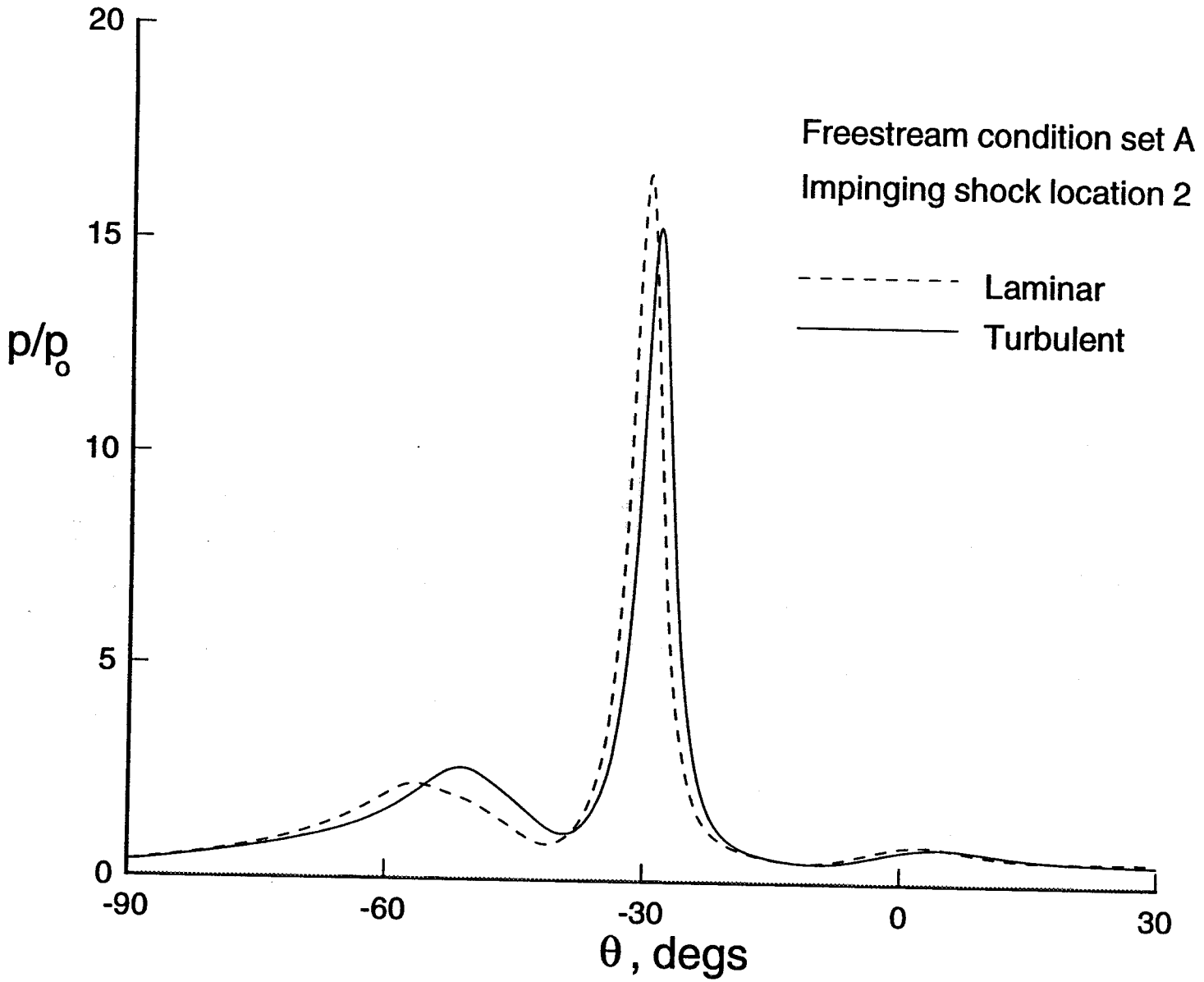

Fig.11b Comparison of the wall pressure distributions from Type IV interference computations at a freestream Reynolds number of 6,500

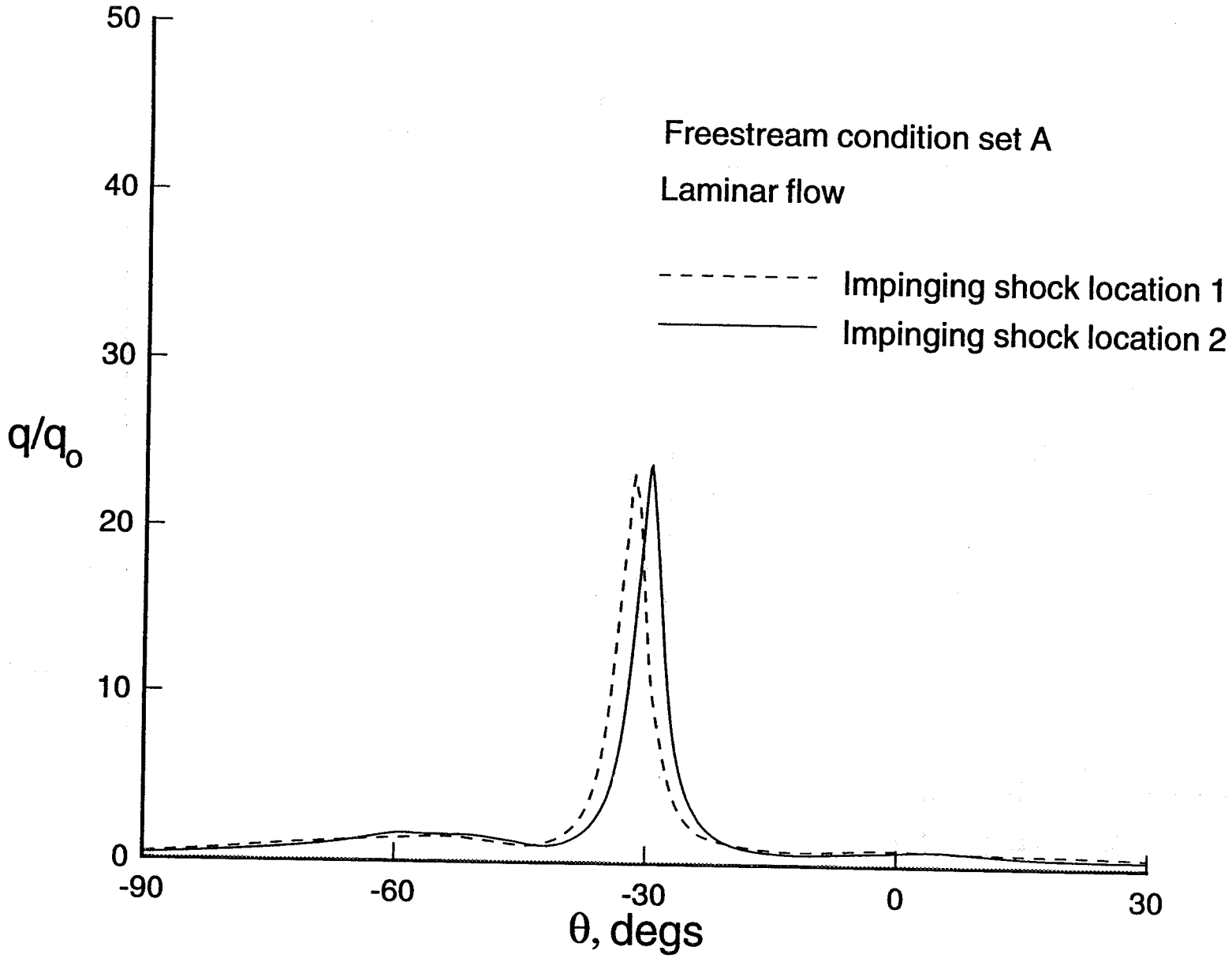

Fig.12a Comparison of the wall heat flux distribution from laminar Type IV interference computations for two impinging shock locations at freestream Reynolds number of 6,500

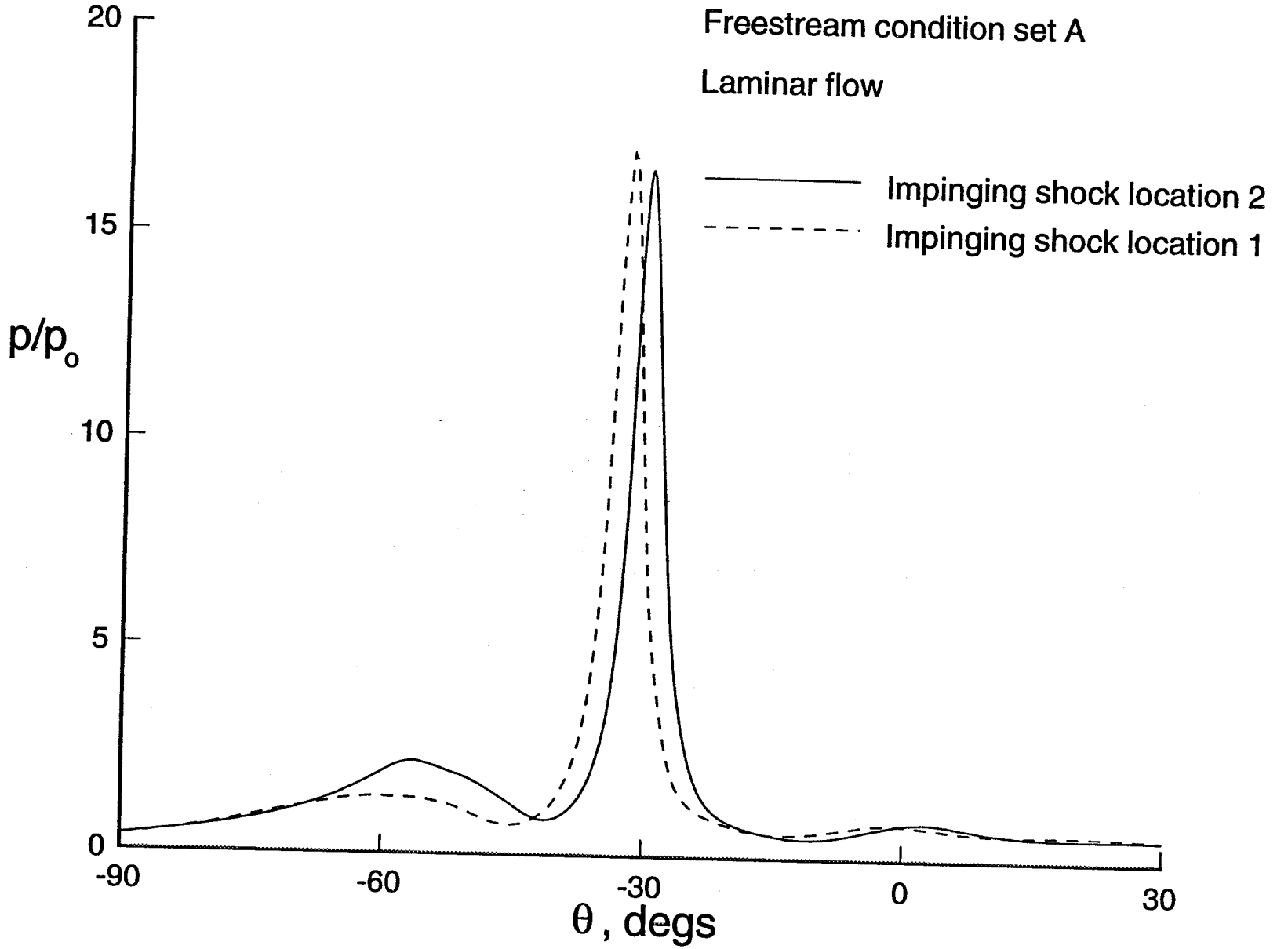

Fig.12b Comparison of the wall pressure distributions from laminar computations of the Type IV interference computations for two impinging shock locations at a freestream Reynolds number of 6,500

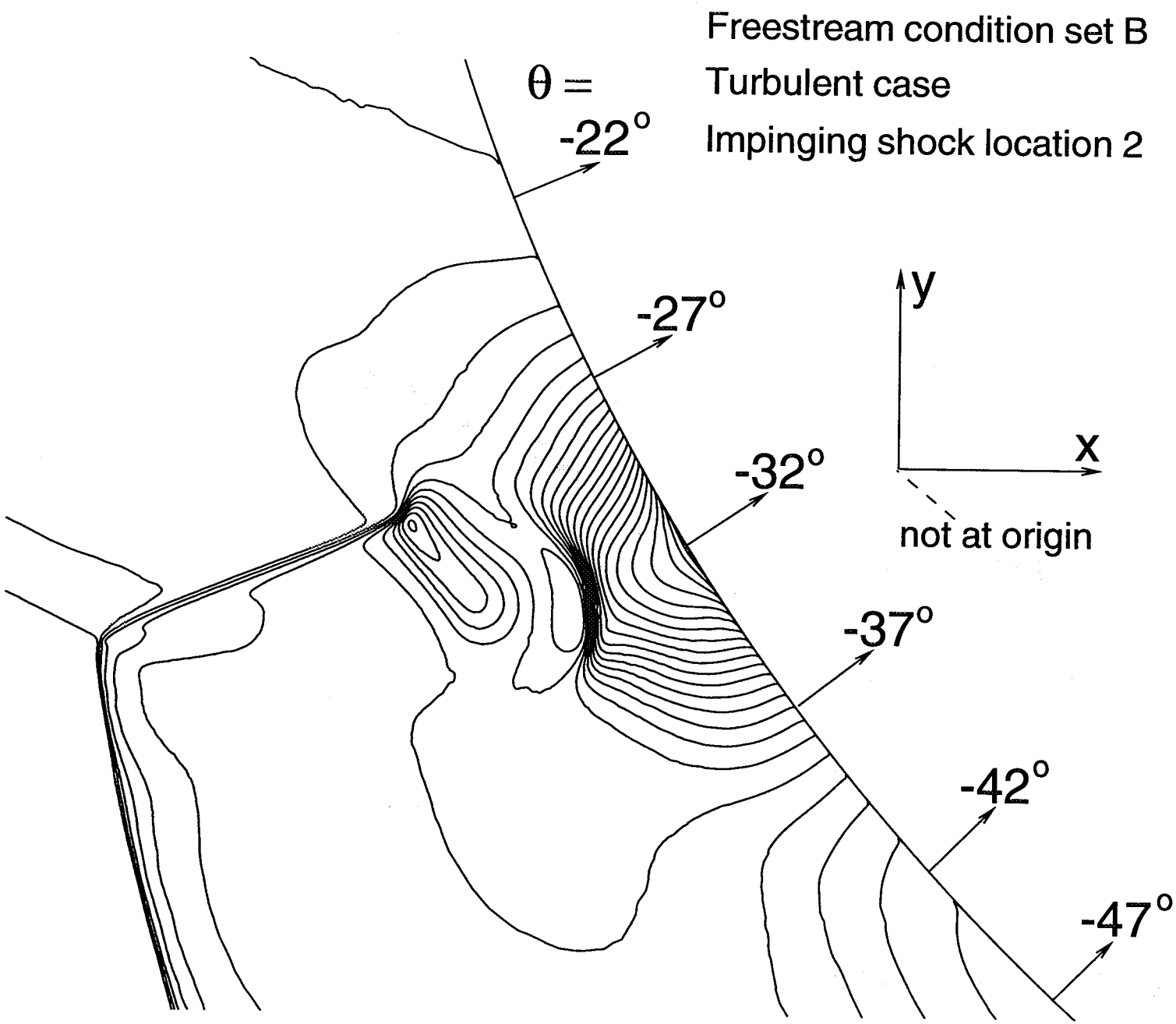

Fig.13 Pressure contours near the stagnation region from the turbulent computations of the Type IV interference at a freestream Reynolds number of 414,000

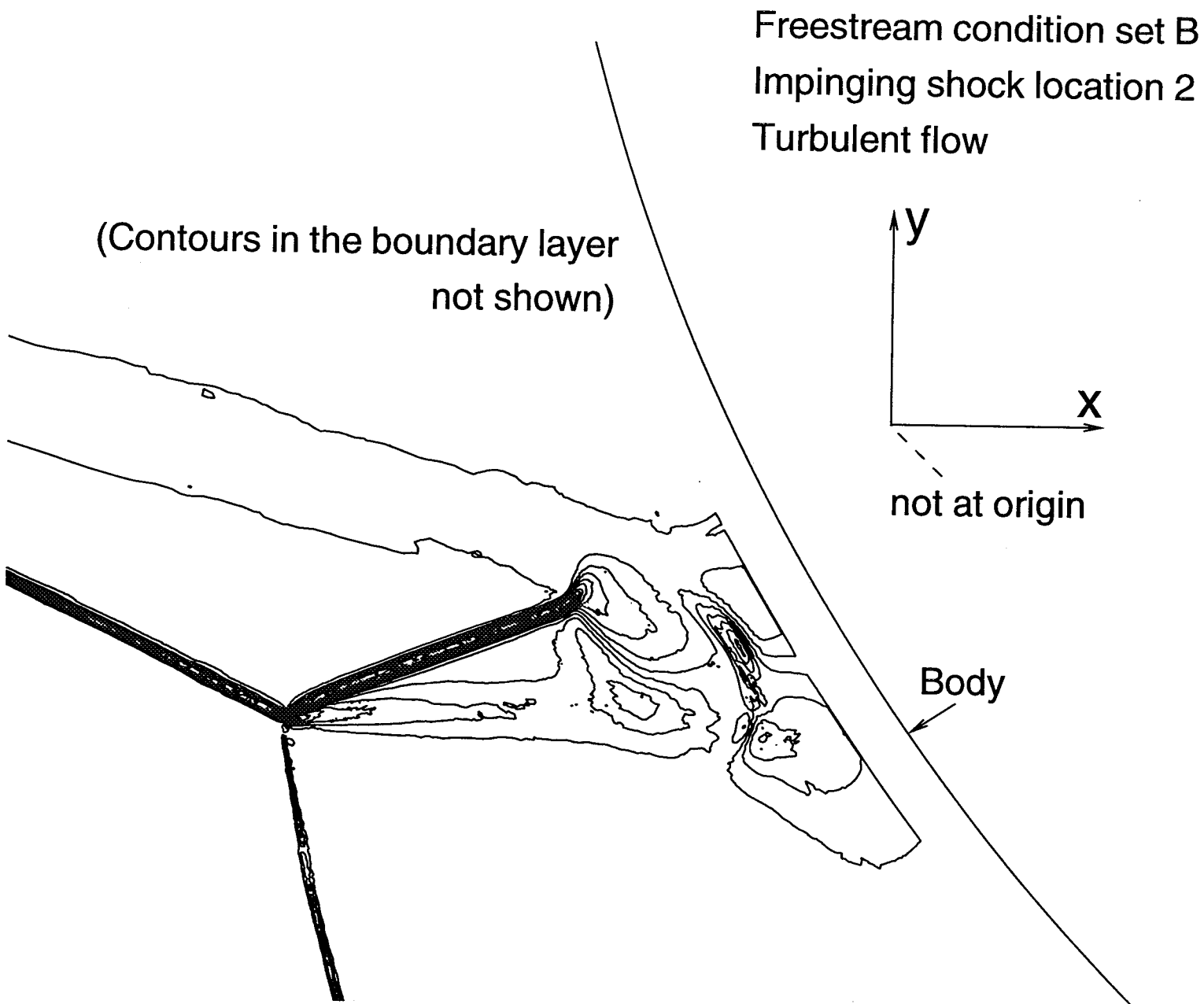

Fig.14 First derivative of density contours near the stagnation region from the LARCNESS computations for the Type IV interference at a freestream Reynolds number of 414,000

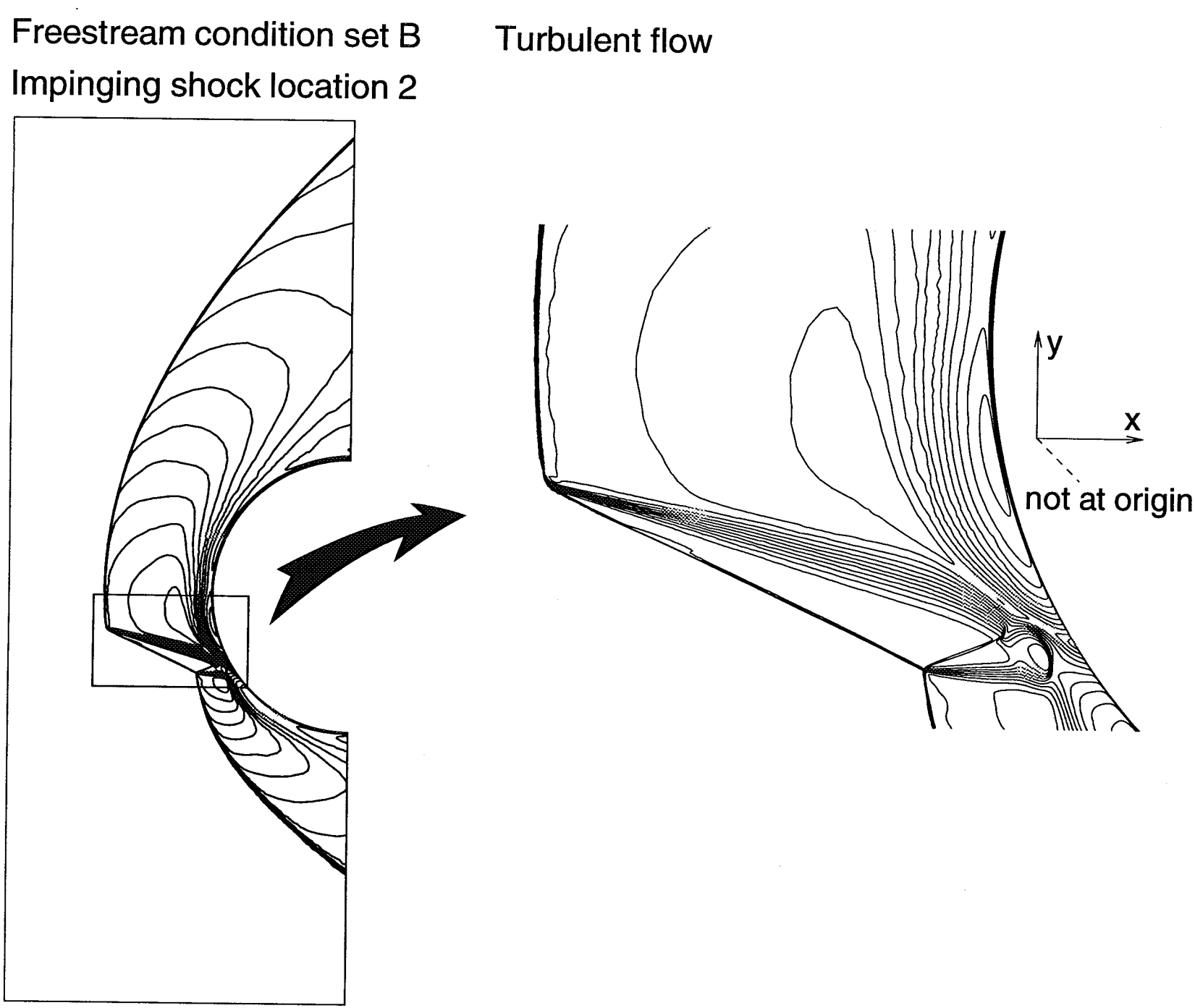

Fig.15a Total velocity contours from the turbulent computations of the Type IV interference at a freestream Reynolds number of 414,000

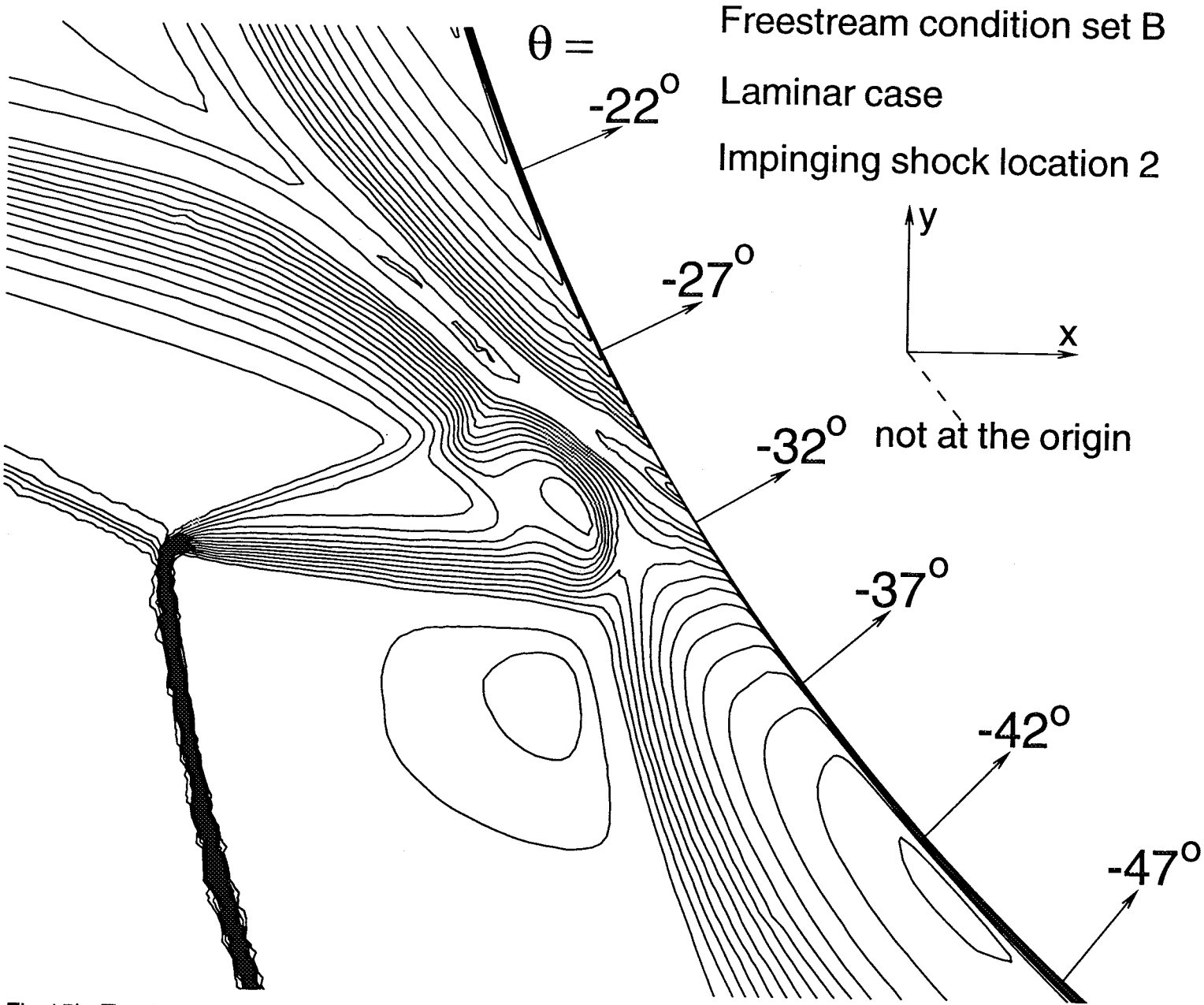

Fig.15b Total velocity contours near the stagnation region from the laminar computations of the Type IV interference at freestream Reynolds number of 414,000

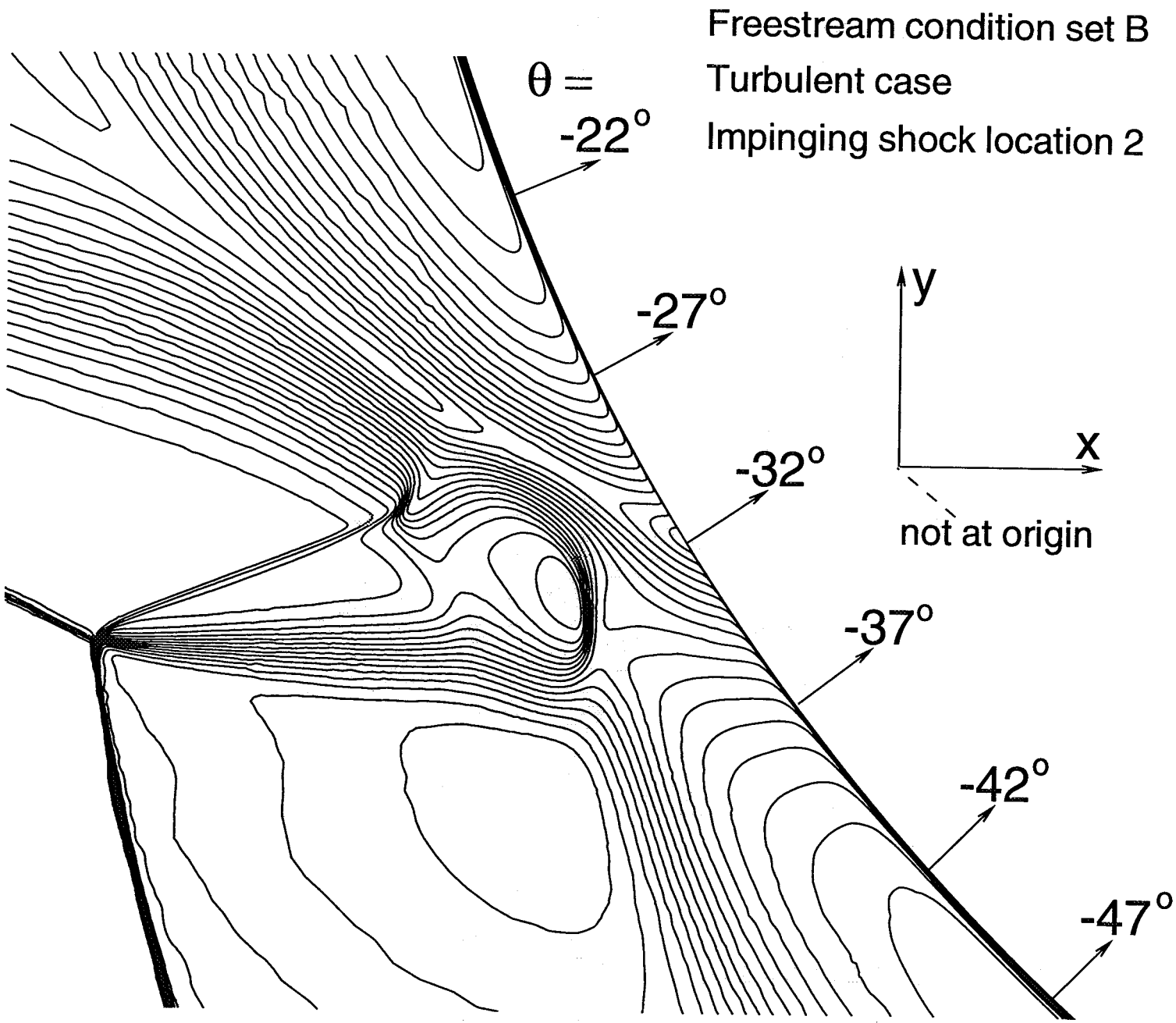

Fig. 15c The total velocity contours near the stagnation region from the turbulent computations of the Type IV interference at a freestream Reynolds number of 414,000

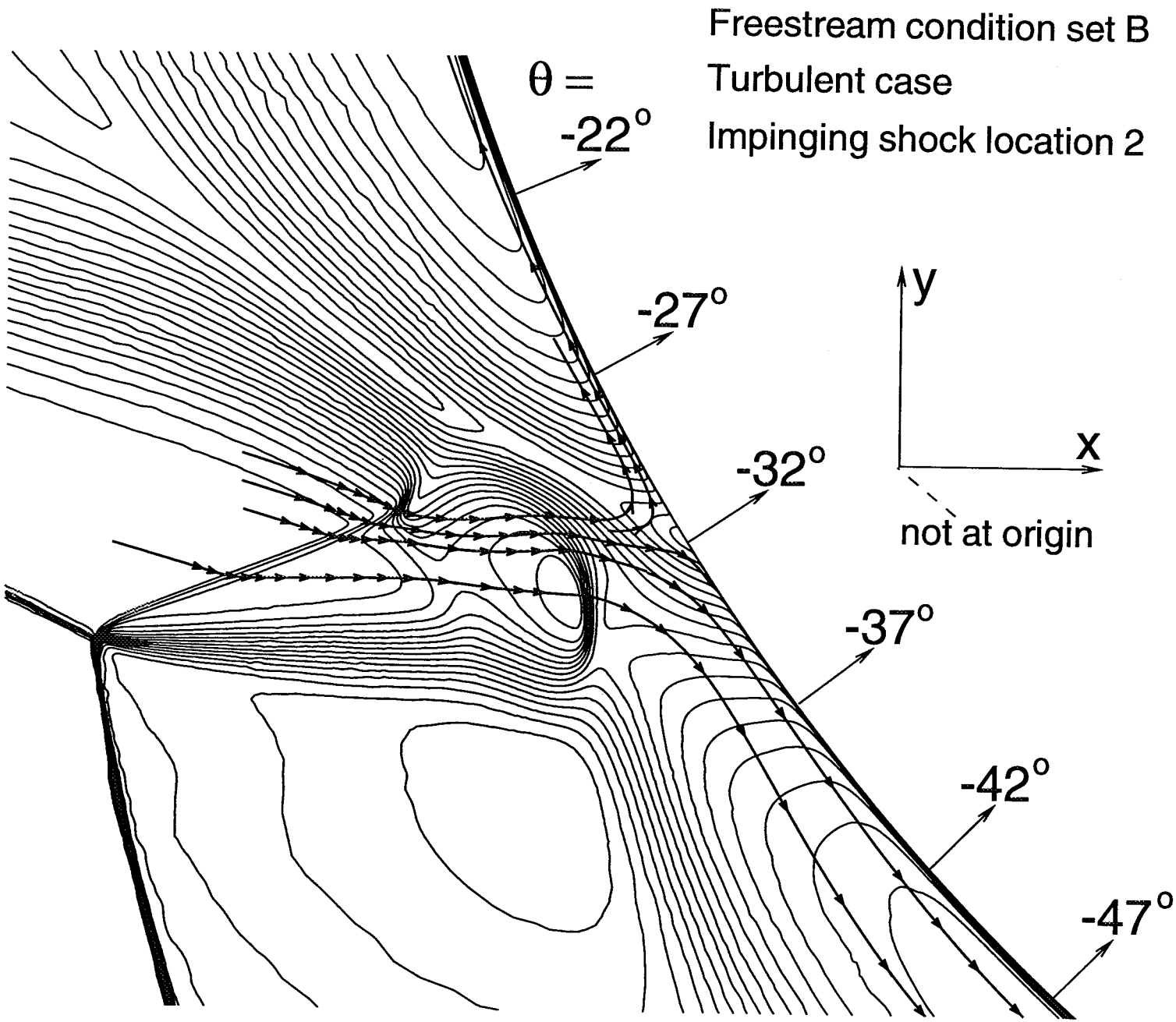

Fig. 16 Streamline contours superimposed on the total velocity contours near the stagnation region from the turbulent computation of the Type IV interference at a freestream Reynolds number of 414,000

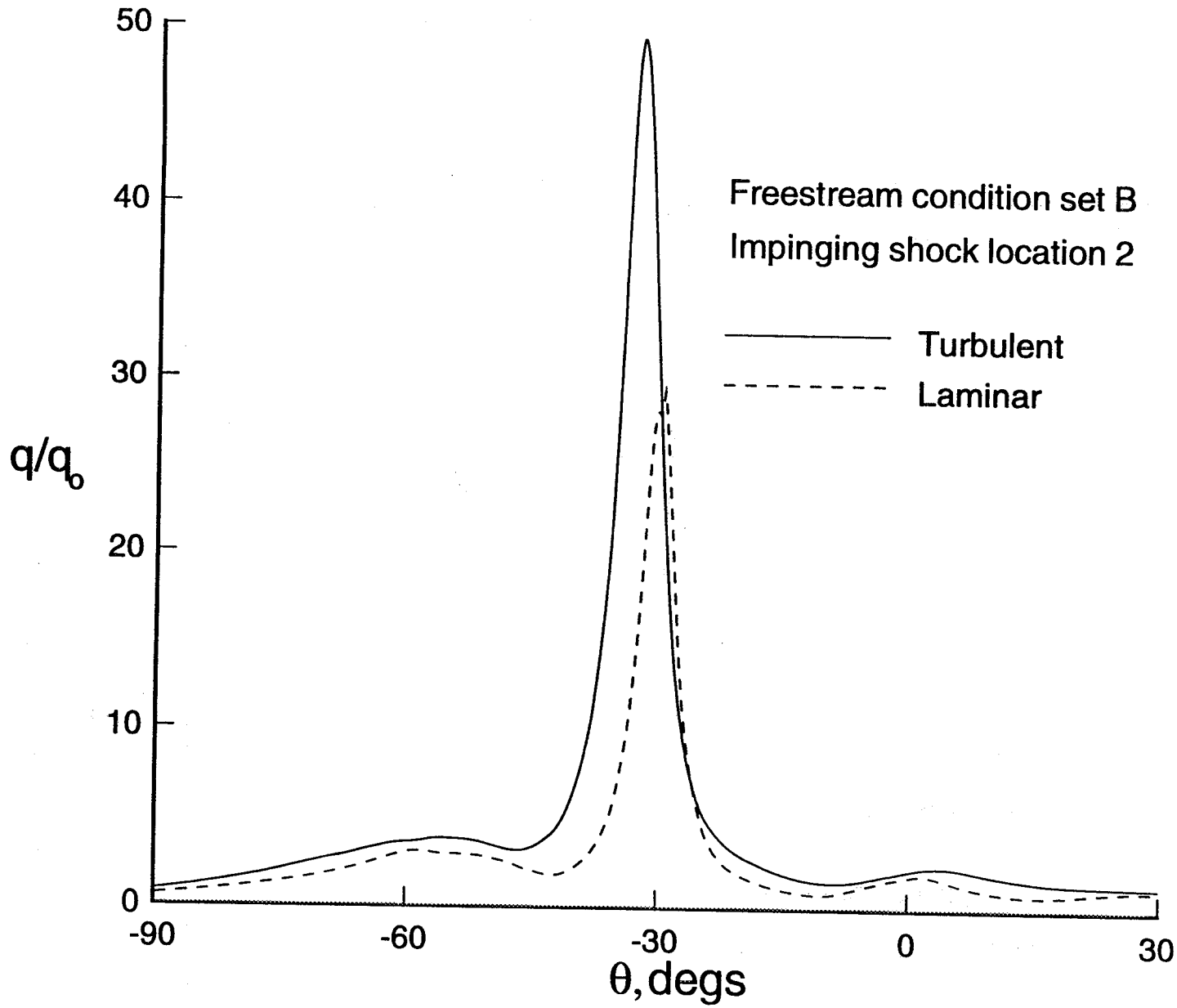

Fig.17a Comparison of laminar and turbulent heat flux distributions from Type IV interference computations at a freestream Reynolds number of 414,000

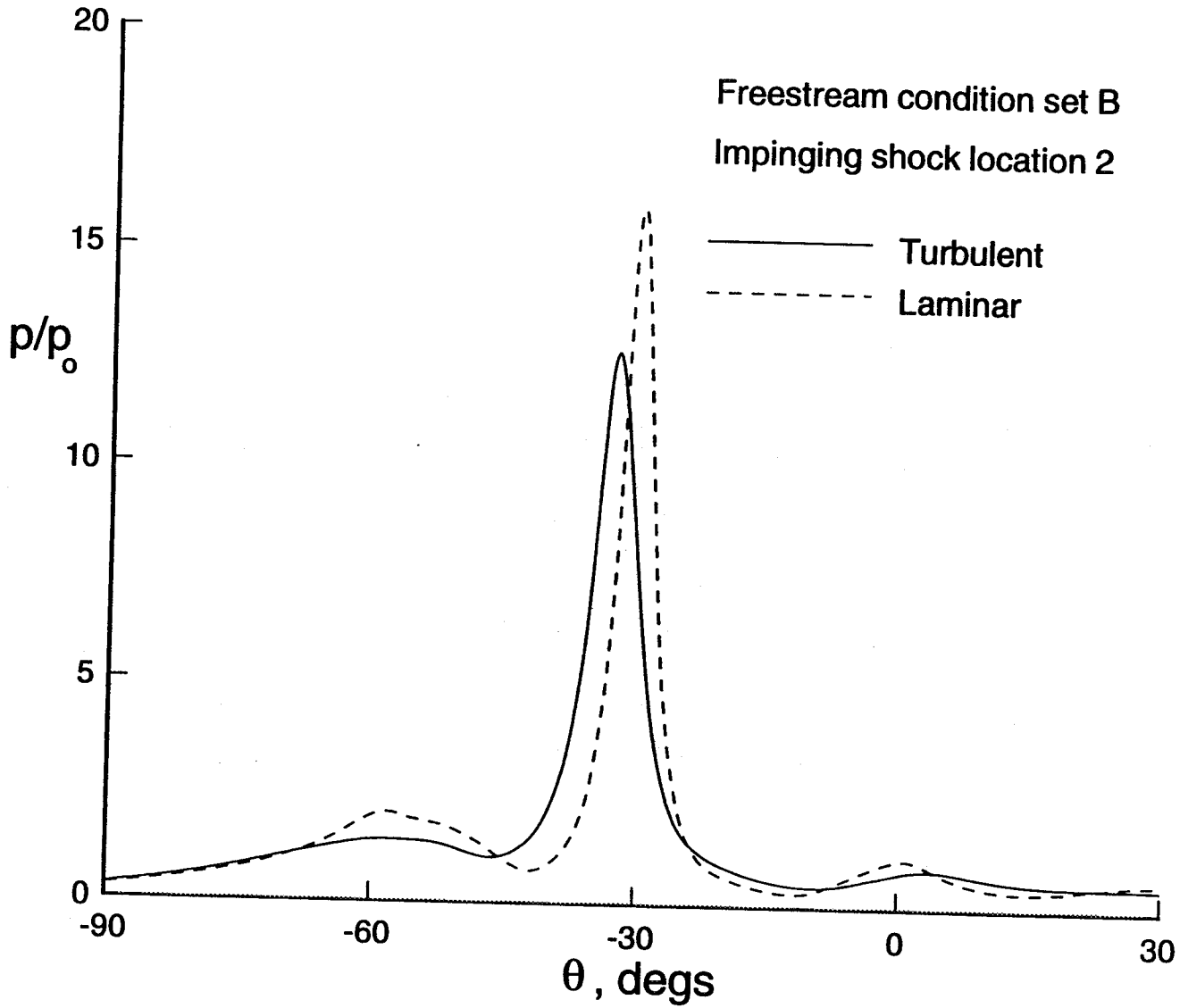

Fig.17b Comparison of laminar and turbulent wall pressure distributions from Type IV interference computations at a freestream Reynolds number of 414,000

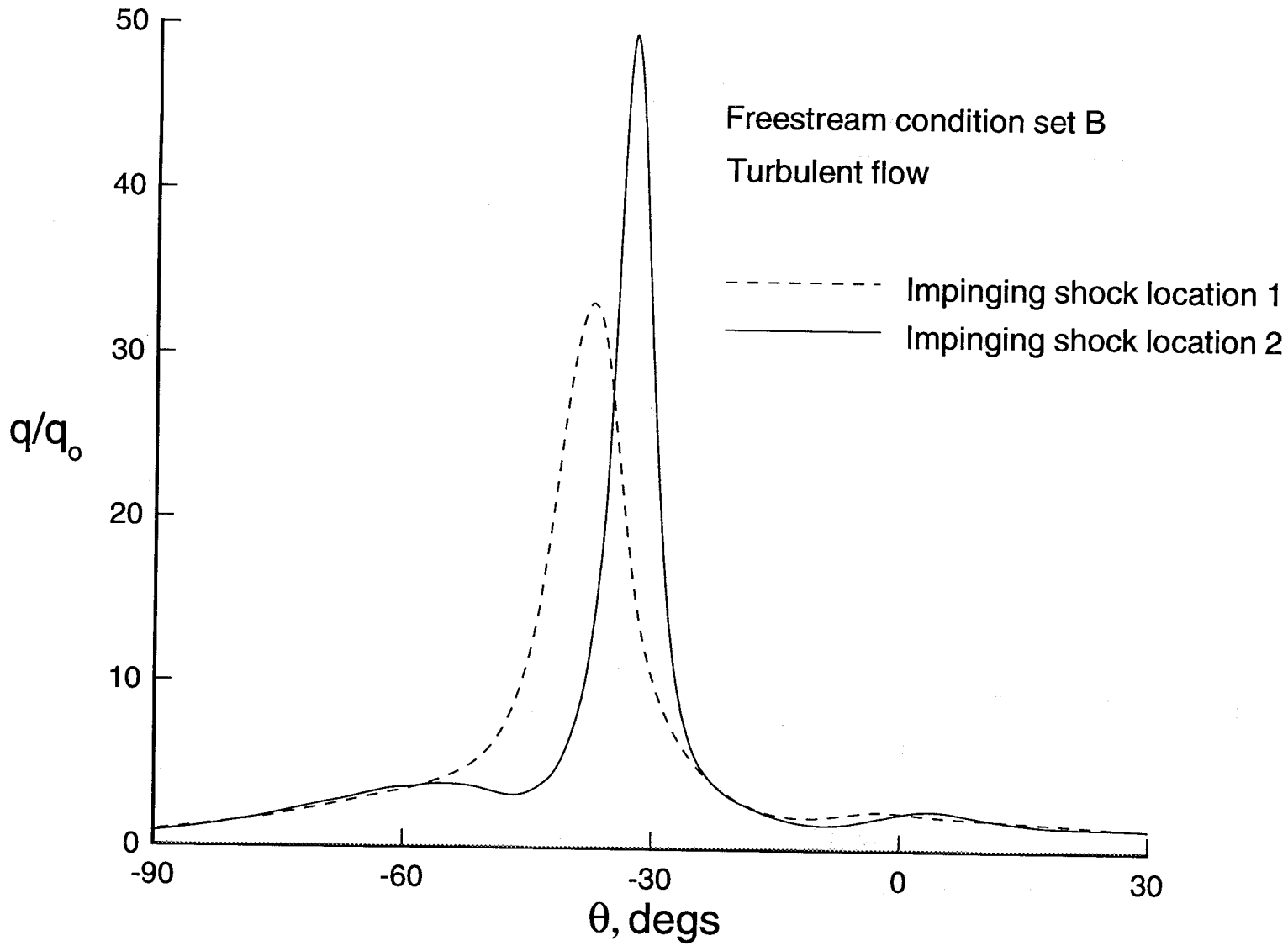

Fig.18a Comparison of wall heat flux distributions from Type IV interference computations for two impinging shock locations at a freestream Reynolds number of 414,000

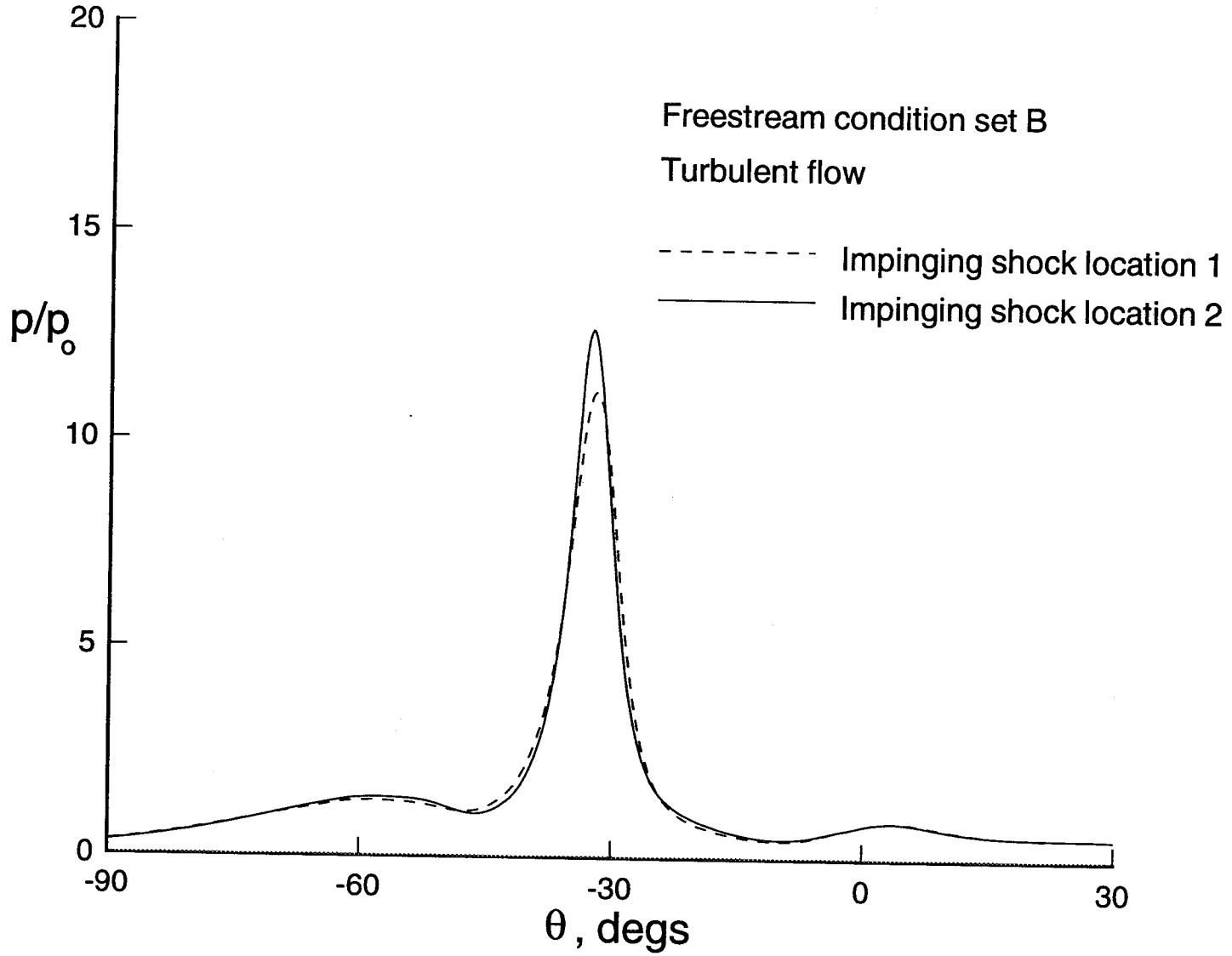

Fig.18b Comparison of wall pressure distributions from Type IV interference computations for two impinging shock locations at a freestream Reynolds number of 414,000

REPORT DOCUMENTATION PAGE

Form Approved
OMB No. 0704-0188

1. AGENCY USE ONLY (Leave blank)	2. REPORT DATE	3. REPORT TYPE AND DATES COVERED
	October 1994	Contractor Report

4. TITLE AND SUBTITLE
Laminar and Turbulent Flow Computations of Type IV Shock-Shock Interference Aerothermal Loads Using Unstructured Grids

5. FUNDING NUMBERS
C NAS1-19000
WU 232-01-04-06

6. AUTHOR(S)
Gururaja R. Vemaganti

7. PERFORMING ORGANIZATION NAME(S) AND ADDRESS(ES)
Lockheed Engineering and Sciences Company
Langley Program Office
144 Research Drive
Hampton, VA 23666

8. PERFORMING ORGANIZATION REPORT NUMBER

9. SPONSORING / MONITORING AGENCY NAME(S) AND ADDRESS(ES)
National Aeronautics and Space Administration
Langley Research Center
Hampton, VA 23681-0001

10. SPONSORING / MONITORING AGENCY REPORT NUMBER
NASA CR-195008

11. SUPPLEMENTARY NOTES
Langley Technical Monitor: Allan R. Wieting

12a. DISTRIBUTION / AVAILABILITY STATEMENT
Unclassified - Unlimited
Subject Category 34

12b. DISTRIBUTION CODE

13. ABSTRACT (Maximum 200 words)
This report presents computations for the Type IV shock-shock interference flow under laminar and turbulent conditions using unstructured grids. Mesh adaptation was accomplished by remeshing, refinement and mesh movement. Two two-equation turbulence models were used to analyze turbulent flows. The mean flow governing equations and the turbulence governing equations are solved in a coupled manner. The solution algorithm and the details pertaining to its implementation on unstructured grids are described. Computations were performed at two different freestream Reynolds numbers at a freestream Mach number of 11. Effects of the variation in the impinging shock location are studied. The comparison of the results in terms of wall heat flux and wall pressure distributions is presented.

14. SUBJECT TERMS
Hypersonic
Laminar and turbulent flows
Shock interference heating
two-equation turbulence models

15. NUMBER OF PAGES
57

16. PRICE CODE
A04

17. SECURITY CLASSIFICATION OF REPORT	18. SECURITY CLASSIFICATION OF THIS PAGE	19. SECURITY CLASSIFICATION OF ABSTRACT	20. LIMITATION OF ABSTRACT
Unclassified	Unclassified		